

University of Dayton

eCommons

Graduate Theses and Dissertations

Theses and Dissertations

2005

Parametric study of the effect of angle of attack and planform geometry variation on the trailing vortex velocity structure behind a flat plate at low Reynolds numbers

Sergey Mikhaylovich Kaplan
University of Dayton

Follow this and additional works at: https://ecommons.udayton.edu/graduate_theses

Recommended Citation

Kaplan, Sergey Mikhaylovich, "Parametric study of the effect of angle of attack and planform geometry variation on the trailing vortex velocity structure behind a flat plate at low Reynolds numbers" (2005). *Graduate Theses and Dissertations*. 3627.
https://ecommons.udayton.edu/graduate_theses/3627

This Thesis is brought to you for free and open access by the Theses and Dissertations at eCommons. It has been accepted for inclusion in Graduate Theses and Dissertations by an authorized administrator of eCommons. For more information, please contact mschlangen1@udayton.edu, ecommons@udayton.edu.

PARAMETRIC STUDY OF THE EFFECT OF ANGLE OF ATTACK AND
PLANFORM GEOMETRY VARIATION ON THE TRAILING VORTEX
VELOCITY STRUCTURE BEHIND A FLAT PLATE
AT LOW REYNOLDS NUMBERS

Thesis

Submitted to

The School of Engineering

UNIVERSITY OF DAYTON

in Partial Fulfillment of the Requirements for

The Degree

Master of Science in Aerospace Engineering

by

Sergey Mikhaylovich Kaplan

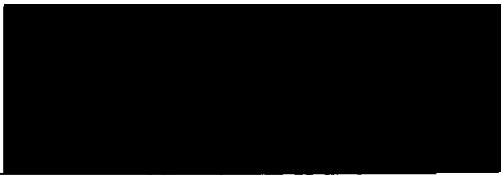
UNIVERSITY OF DAYTON

Dayton, Ohio

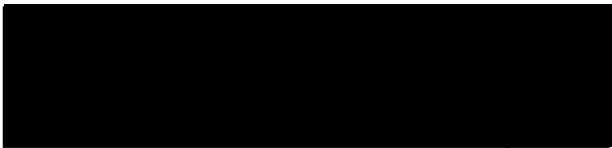
August, 2005

PARAMETRIC STUDY OF THE EFFECT OF ANGLE OF ATTACK AND
PLANFORM GEOMETRY VARIATION ON THE TRAILING VORTEX VELOCITY
STRUCTURE BEHIND A FLAT PLATE AT LOW REYNOLDS NUMBERS

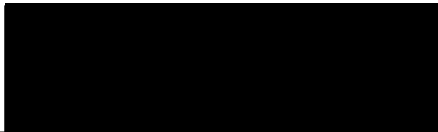
APPROVED BY:




Aaron Altman, Ph.D.
Advisory Committee Chairman
Associate Professor, Mechanical and
Aerospace Engineering Department



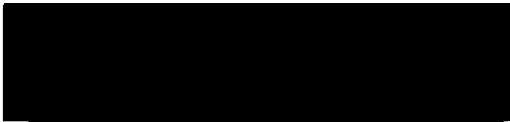
Timothy J. Fry, Ph.D.
Committee Member
Associate Professor, Mechanical and
Aerospace Engineering Department



Kevin P. Hallinan, Ph.D.
Committee Member
Professor and Chairperson
Mechanical and Aerospace Engineering Department



Donald L. Moon, Ph.D.
Associate Dean
Graduate Engineering Programs & Research
School of Engineering



Joseph E. Saliba, Ph.D., P.E.
Dean, School of Engineering

ABSTRACT

PARAMETRIC STUDY OF THE EFFECT OF ANGLE OF ATTACK AND PLANFORM GEOMETRY VARIATION ON THE TRAILING VORTEX VELOCITY STRUCTURE BEHIND A FLAT PLATE AT LOW REYNOLDS NUMBERS

Name: Kaplan, Sergey, Mikhaylovich

University of Dayton

Advisor: Dr. Aaron Altman

Velocity structure of the trailing wingtip vortex at low Reynolds numbers (1,000 to 25,000) is studied experimentally to determine if the relationships at low Reynolds numbers between vortex structure and strength, and coefficient of lift for different planform geometries and angles of attack are the same as the relationships that apply to high Reynolds number flows. Except for delta wings, very little research has been performed to study the effects of variations in basic parameters such as angle of attack and planform geometry on the trailing vortex tangential velocity or vorticity at low Reynolds numbers. Thus, very little is understood about the quasi-steady-state aerodynamics of even simple structures like flat plates and how the velocity and structure of the trailing vortex are affected by variations in basic geometric parameters at low Reynolds numbers. In this study, the angle of attack is systematically varied for three different planform geometries, a rectangle, an ellipse and a delta, given a constant thickness, aspect ratio, span, mean aerodynamic chord and area of all three flat plates in a water tunnel. With the choice of mean chord and flow speeds, these characteristics produce low Reynolds numbers ranging from 1,000 to 25,000. The impact of the variations on the wingtip trailing vortex tangential velocity and structure, as well as vorticity in the near wake of the vortex itself is measured through the use of digital particle image velocimetry (PIV) to determine whether, in keeping with previously

developed theory at high Reynolds numbers, the velocity structure of the vortex changes with variation in each of the aforementioned parameters. Interestingly enough, despite low Reynolds number flow, where viscous forces dominate, there is minimal effect on the dissipation of vortices behind flat plates. Thus, classical theoretical predictions of the coefficient of lift and angle of attack relationships for high Reynolds number flows, which are based on inviscid flow assumptions, can be applied at low Reynolds numbers from 1,000 to 25,000.

ACKNOWLEDGEMENTS

I would like to thank Dr. Aaron Altman for his leadership and mentorship in my academic ventures over the past two years. He has given me enough freedom and time to finish this study and was there to provide much needed direction. I would like to also thank Dr. Michael Ol for providing me access to the testing facility and for enormous amount of time he spent helping me obtain the data used in this study. Writing this paper would not have been possible without his efforts and support.

Finally, I would like to thank my family who helped me through some uncertain times not just during the past two years, but also throughout my entire life.

TABLE OF CONTENTS

ABSTRACT.....	III
ACKNOWLEDGEMENTS.....	V
LIST OF ILLUSTRATIONS.....	VIII
LIST OF TABLES.....	X
LIST OF SYMBOLS.....	XI
INTRODUCTION.....	1
CHAPTER.....	3
I. VORTEX THEORY.....	3
1.A. VORTEX STRUCTURE.....	3
1.B. VORTICITY AND CIRCULATION.....	4
1.C. THEORY.....	6
1.D. PRANDTL'S CLASSICAL LIFTING-LINE THEOREM.....	8
1.E. COEFFICIENT OF LIFT THEORETICAL APPROXIMATIONS.....	9
II. LITERATURE REVIEW.....	13
2.A. REAL-WORLD APPLICATION.....	13
2.B. PAPER REVIEW.....	14
2.C. EXPECTED RELATIONSHIPS BETWEEN THEORY AND EXPERIMENTAL DATA ...	20
III. DIGITAL PARTICLE IMAGE VELOCIMETRY.....	22
3.A. COMPONENTS AND SET-UP.....	22
3.B. TIMING AND THEORY.....	23
IV. EMPLOYED METHODS.....	25
4.A. CAMERA MOUNTED AFT.....	25
4.B. VIEWING THROUGH A PRISM.....	27
4.C. MIRROR APPLICATION.....	28
4.E. COORDINATE SYSTEM.....	30
4.D. FLOW VISUALIZATION.....	31
V. TESTS AND ANALYSIS.....	33
5.A. MODELS.....	33
5.B. TEST FACILITY AND EQUIPMENT.....	35

5.C. DATA GATHERING	37
5.D. POST-PROCESSING AND ANALYSIS	38
VI. RESULTS	45
6.A. FLOW VISUALIZATION	45
6.B. VELOCITY AND VORTICITY OBSERVATIONS.....	48
6.C. COEFFICIENT OF LIFT COMPARISON	60
VII. CONCLUSIONS	64
VIII. RECOMMENDATIONS	67
BIBLIOGRAPHY	68

LIST OF ILLUSTRATIONS

Figure 1: Reynolds number relationship to maximum coefficient of lift.....	1
Figure 2: Airfoil generating vortices.....	3
Figure 3: Circulation.....	6
Figure 4: Superposition of vortices on the lifting line.....	8
Figure 5: Induced velocity; Vortex lattice method.....	11
Figure 6: DPIV Set-up.....	22
Figure 7: DPIV timing scheme.....	23
Figure 8: Camera behind a window at the end of the tunnel.....	25
Figure 9: Astigmatism with camera in the back.....	26
Figure 10: Camera mounted at 45 degrees to the plane of interest.....	27
Figure 11: Camera at an angle to the plane of interest set-up.....	28
Figure 12: PIV set-up using the mirror.....	29
Figure 13: Rectangular wing; 10 deg. AoA; downstream $X/C = 1/10$; $U_{\infty} = 9$ cm/s; $Re = 8,028$;	29
Figure 14: Coordinate System.....	30
Figure 15: True orientation of the models.....	32
Figure 16: Delta wing; Dimensions in centimeters.....	33
Figure 17: Rectangular wing; Dimensions in centimeters.....	34
Figure 18: Elliptical wing; Dimensions in centimeters.....	34
Figure 19: Water tunnel.....	35
Figure 20: Rectangular wing; 10 deg. AoA; downstream $X/C = 1/10$; $U_{\infty} = 9$ cm/s; $Re = 8,028$;	39
Figure 21: Rectangular wing; 10 deg. AoA; downstream $X/C = 1/10$; $U_{\infty} = 9$ cm/s; $Re = 8,028$;	40
Figure 22: Outliers for delta wing; 10 deg. AoA; downstream $X/C = 1/10$; $U_{\infty} = 27$ cm/s; $Re = 24,083$;	41
Figure 23: Rectangular wing; 10 deg. AoA; downstream $X/C = 1/10$; $U_{\infty} = 9$ cm/s; $Re = 8,028$;	42
Figure 24: Rectangular wing; 10 deg. AoA; downstream $X/C = 1/10$; $U_{\infty} = 9$ cm/s; $Re = 8,028$; a) Orientation as tested; b) Inverted vortex;	42
Figure 25: Rectangular wing; 10 deg. AoA; downstream $X/C = 1/10$; $U_{\infty} = 9$ cm/s; $Re = 8,028$; Circulation;	43
Figure 26: Rectangular wing; 5 deg. AoA; $Re = 8,028$; Flow visualization;	45
Figure 27: Delta wing; 10 deg. AoA; $Re = 8,028$; Flow visualization;	46
Figure 28: Elliptical wing; 5 deg. AoA; $Re = 8,028$; Flow visualization;	47
Figure 29: Velocity and Vorticity; 10 deg. AoA; downstream $X/C = 1$; $U_{\infty} = 27$ cm/s; $Re = 24,083$; DPIV results;	49
Figure 30: Velocity and Vorticity; 15 deg. AoA; downstream $X/C = 1$; $U_{\infty} = 27$ cm/s; $Re = 24,083$; DPIV results;	50

Figure 31: Velocity and Vorticity; 10 deg. AoA; downstream $X/C = 1$; $U_{\infty} = 27$ cm/s; $Re = 8,028$; DPIV results;	50
Figure 32: Individual image pairs; 15 deg. AoA; downstream $X/C = 1$; $Re = 24,083$;	51
Figure 33: Normalized Circulation at downstream $X/C = 1$;	52
Figure 34: Vortex comparison with distance downstream from trailing edge; Rectangle at 10 deg. AoA;	53
Figure 35: Vortex comparison with distance downstream from trailing edge; Delta at 10 deg. AoA;	53
Figure 36: Vortex comparison with distance downstream from trailing edge; Ellipse at 10 deg. AoA;	54
Figure 37: C_l vs. X/C Comparison for Rectangle	54
Figure 38: C_l vs. X/C Comparison for Delta.....	55
Figure 39: C_l vs. X/C Comparison for Ellipse	55
Figure 40: Vortex position downstream of the trailing edge; Rectangle	57
Figure 41: Vortex position downstream of the trailing edge; Delta.....	57
Figure 42: Vortex position downstream of the trailing edge; Ellipse	58
Figure 43: C_l vs. AoA curve; Rectangle	60
Figure 44: C_l vs. AoA curve; Delta.....	61
Figure 45: C_l vs. AoA curve; Ellipse	62

LIST OF TABLES

Table 1: Flow visualization test matrix.....	37
Table 2: DPIV test matrix.....	38
Table 3: Coefficient of lift error compared to Laitone's force balance measurements	61
Table 4: Coefficient of lift error compared to theoretical predictions	62

LIST OF SYMBOLS

U_∞	=	freestream velocity
ω	=	vorticity
ω_x	=	vorticity in yz plane
ξ	=	angular velocity
\mathbf{V}	=	velocity field vector
V	=	velocity in yz plane
C	=	closed curve
Γ	=	circulation
$\bar{\Gamma}$	=	normalized circulation
L'	=	lift per unit span
L	=	lift
ρ_∞	=	density
S	=	area
b	=	span
c	=	chord
\bar{c}	=	mean aerodynamic chord
c_l	=	coefficient of lift based on lift per unit span
C_l	=	coefficient of lift
α , AoA	=	angle of attack
α_i	=	induced angle of attack
AR	=	aspect ratio
$\phi_{1/2c}$	=	midchord line sweep angle
t	=	time
Δt	=	difference in time
X/C	=	distance downstream of the trailing edge

INTRODUCTION

Fundamental relationships already exist to predict the most basic characteristics of an airfoil or even a flat plate at Reynolds numbers greater than 25,000. Calculation and prediction of these relationships are based on the assumptions of an inviscid flow, where viscous forces are considered insignificant. The coefficient of lift based on the angle of attack, planform geometry and wake structure behind a lifting body are among some of these most rudimentary relationships that must be understood before venturing into aerodynamics and conventional aircraft design. However, few studies have been performed in order to understand the crucial interaction between viscous and momentum forces and thus, to predict very basic airfoil characteristics such as the coefficient of lift at low Reynolds numbers, in the range of 1,000 to 25,000, where viscous forces dominate.

Mueller shows that for smooth airfoils, maximum coefficient of lift dramatically increases between the Reynolds numbers of 10,000 and 100,000, as seen in Figure 1.¹

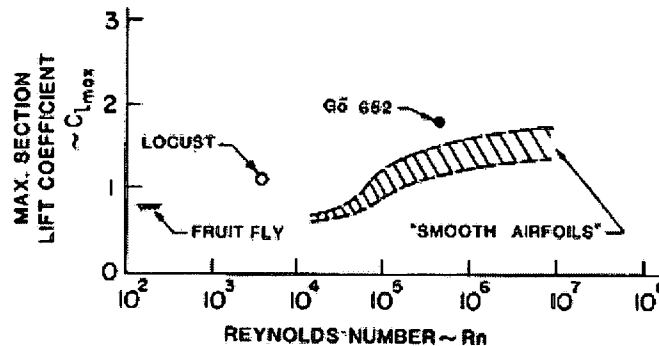


Figure 1: Reynolds number relationship to maximum coefficient of lift

This increase may indicate that laminar flows around airfoils at low Reynolds numbers may not necessarily be as desirable, as is commonly assumed at high Reynolds numbers. However, there is little understanding of the basic relationship between the coefficient of lift and angle of attack as well as its relation to the trailing vortex strength at low

Reynolds numbers between 1,000 and 25,000. Therefore, this study focuses on understanding the connection between the coefficient of lift, experimentally obtained from studying trailing vortex structure, and circulation at low Reynolds numbers (1,000 - 25,000), and theoretical predictions based on inviscid flow assumptions for flat plates with different planform geometry at high Reynolds numbers ($>25,000$). Trailing vortex roll-up and formation behavior at low Reynolds numbers is also observed with the help of flow visualization. It is important to note that in this study, coefficient of lift is calculated using Kutta-Joukowski Theorem after obtaining circulation based on the velocity field in the cross-flow plane with the help of the digital particle image velocimetry technique.

CHAPTER I

VORTEX THEORY

1.a. Vortex Structure

As any wing is immersed into airflow and produces lift, there is a tendency to create a circulatory flow from the higher to lower pressure regions at the wing tip. The flow that is created is the rotational velocity field on the spanwise ends of the body and is called a wingtip vortex. The chordwise movement of the airfoil through the fluid generates two vortices, one on each end of the body (wing), downstream from the wingtip to infinity, called the trailing vortex as seen in Figure 2.

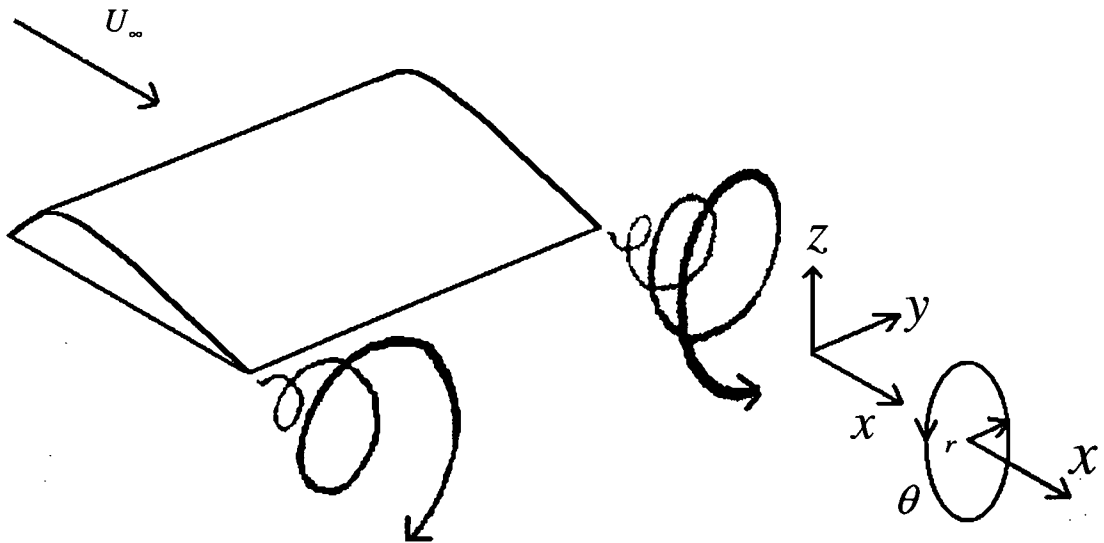


Figure 2: Airfoil generating vortices

The trailing wingtip vortex is made up of the axial velocity component, parallel to freestream, and spanwise flow component, from the root of the body to the wingtip. The trailing wing tip vortex also has two distinct regions. The first region is the vortex core, where circulation is near constant spanwise and is at its maximum value. The vortex core

is also the region where the axial velocity in the vortex is at a maximum value and in some cases, depending on the angle of attack, is greater than the freestream velocity by up to 70%.² The second region is the outer region of the vortex, where spanwise variations in circulation strength are largely dominated by viscous effects. The characteristics of this region dictate the dissipation properties of the trailing vortex both in space and time. The outer region also hosts secondary vortices, which over time dissipate or join the primary vortex. The strength, layout and characteristics of secondary vortices can prohibit analysis of the main vortex, if an averaging method of measurement is used to calculate the strengths of all the wing tip vortices. Thus in reality, depending on the stability and longevity of the primary vortex as well as secondary vortices, statistical analysis of circulation and velocity structure may produce poor or unreliable results.

1.b. Vorticity and Circulation

Navies-Stokes equations are the most fundamental representation of viscous fluid flow. Using the momentum equation, for Newtonian viscous fluid, Navier-Stokes equations are shown in Eq. 1 in a single vector form, assuming constant viscosity and density.

$$\rho \frac{D\mathbf{V}}{Dt} = \rho \mathbf{g} - \nabla p + \mu \nabla^2 \mathbf{V} \quad (1)$$

In Eq.1, \mathbf{g} is gravity, μ is viscosity, p is pressure, ρ is density and \mathbf{V} is velocity field vector. Taking a divergence of the entire Eq.1 to eliminate \mathbf{V} , and taking the curl to eliminate the pressure term, the result is presented by Eq. 2.

$$\frac{\partial \boldsymbol{\omega}}{\partial t} = \frac{\mu}{\rho} \nabla^2 \boldsymbol{\omega} \quad \text{where } \boldsymbol{\omega} = \text{curl } \mathbf{V} = \text{fluid vorticity} \quad (2)$$

Angular velocity is also related to fluid vorticity, which in turn is related to circulation. However, because the coefficient of lift is calculated from circulation, the fundamentals of angular velocity must be defined and understood before looking at the aerodynamic parameters of interest. If we consider an infinitesimal fluid element that moves along a streamline, we can also take into account the extent to which the element

is distorted or rotated.³ The amount of such distortion is dependent on the angular velocity of the flow field, which is presented by Eq. 3:

$$\boldsymbol{\omega} = \frac{1}{2} \left[\left(\frac{\partial w}{\partial y} - \frac{\partial v}{\partial z} \right) \mathbf{i} + \left(\frac{\partial u}{\partial z} - \frac{\partial w}{\partial x} \right) \mathbf{j} + \left(\frac{\partial v}{\partial x} - \frac{\partial u}{\partial y} \right) \mathbf{k} \right] \quad (3)$$

The components w , v and u are velocities in z , y and x directions respectively as seen in Figure 2. Since, we are interested only in the two-dimensional cross-flow plane, in particular the yz plane, the angular velocity is presented by Eq. 4:

$$\omega_x = \frac{1}{2} \left(\frac{\partial w}{\partial y} - \frac{\partial v}{\partial z} \right) \quad (4)$$

Vorticity is defined by nothing more than twice the amount of angular velocity, namely:

$$\boldsymbol{\xi} = \left(\frac{\partial w}{\partial y} - \frac{\partial v}{\partial z} \right) \mathbf{i} + \left(\frac{\partial u}{\partial z} - \frac{\partial w}{\partial x} \right) \mathbf{j} + \left(\frac{\partial v}{\partial x} - \frac{\partial u}{\partial y} \right) \mathbf{k} = \nabla \times \mathbf{V} \quad (5)$$

where \mathbf{V} is the velocity field vector. In two dimensions vorticity is once again defined in Eq. 6:

$$\xi_x = \left(\frac{\partial w}{\partial y} - \frac{\partial v}{\partial z} \right) \quad (6)$$

Thus in a velocity field, vorticity is defined as the curl of the velocity vector.⁴

To define circulation, we consider a closed curve C in a flow field and we let \mathbf{V} be velocity and $d\mathbf{s}$ be the tangential line segment at a point on C . The circulation Γ is simply the negative of the line integral of velocity around a closed curve in the flow:⁵

$$\Gamma = - \int_C \mathbf{V} \cdot d\mathbf{s} \quad (7)$$

Thus circulation depends only on the velocity field and the chosen point on C .

Circulation is also related to vorticity where circulation is defined as vorticity integrated over surface area bounded by the closed curve C as presented below in Eq. 8⁶:

$$\Gamma = - \iint_S (\nabla \times \mathbf{V}) \cdot d\mathbf{s} \quad \text{or} \quad (\nabla \times \mathbf{V}) \cdot \mathbf{n} = - \frac{d\Gamma}{dS} \quad (8)$$

Graphically, the definition of circulation as it relates to vorticity is presented in Figure 3.

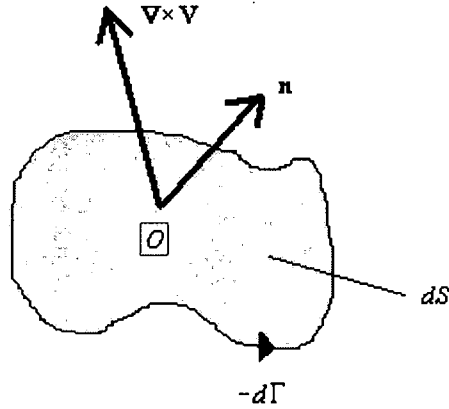


Figure 3: Circulation

This definition is very important, because it will be used later to determine the circulation of the wing-tip vortices in the yz plane to correlate the circulation with the estimated lift generated by the models using the Kutta-Joukowski theorem.

1.c. Theory

For the inviscid and incompressible flow, Kutta-Joukowski theorem states that lift per unit span, L' , is directly proportional to circulation as seen in Eq. 9⁷:

$$L' = \rho_{\infty} U_{\infty} \Gamma \quad (9)$$

where ρ_{∞} is the density and U_{∞} is freestream velocity. Also, based on the span b , the chord c and the wing area S , definition for the coefficient of lift, C_l , is given by Eq. 10:

$$C_l = \frac{L}{q_{\infty} S} \quad \text{where: } q_{\infty} = \frac{1}{2} \rho_{\infty} U_{\infty}^2 \quad \text{and } S = bc \quad (10)$$

Thus, although the viscous effects at high Reynolds numbers are much smaller compared to the momentum effects, and this classical theory can be applied to the wings immersed in high Reynolds number flows, in our case it will be interesting to see how Kutta-Joukowski theorem can be applied to estimate the vortex strength and the equivalent lift produced by a flat plate at low Reynolds numbers, where the viscous forces generally dominate the flow characteristics.

The Kutta condition states that the circulation around an airfoil is such that the flow “leaves the trailing edge smoothly without viscous effects”, namely the velocities shed off the top and bottom of the airfoil are equal in magnitude and direction.⁸

According to Kelvin's circulation theorem, the time rate of change of circulation around a closed curve, which consists of the same fluid elements, is zero:⁹

$$\frac{D\Gamma}{Dt} = 0 \quad (11)$$

Also, from the interpretation of Kelvin's circulation theorem, circulation around the airfoil is equal and opposite to the circulation around a starting vortex, which is shed downstream of the trailing edge. When the starting vortex builds up to equal but opposite strength as the circulation generated by the airfoil, the Kutta condition is satisfied and the balance of the two circulations creates a steady vortex.¹⁰ This vortex will be studied in this experiment and its effects on lift will be observed at low Reynolds numbers, where once again, viscous forces dominate the flow.

To compare the experimental coefficients of lift to the theoretical values, we first have to define approximations or solutions, which will work for all three models. This is a subject of interest, since all of the theories that will be used for comparison are not related to the Reynolds number in their development and do not take it into account. Since there is much experimental data to prove that these classical solutions hold for high Reynolds number flows, where momentum forces dominate the viscous forces, this experiment is geared to find out if the same relationships hold for the low Reynolds number flows, where the domination is opposite. However, no single theory or approximation covers rectangular low aspect ratio, delta and elliptical planform geometries. Thus different classical theories will be applied to each model, to see how the coefficient of lift calculated from the relationship between lift, circulation and coefficient of lift definitions given by Kutta-Joukowski theorem, are compared to these theoretical predictions.

The first and most simple approximation is the classical thin symmetric airfoil theory. According to this theory, where total circulation is integrated along a chord line, with assumptions of inviscid, incompressible flow over a flat plate at an angle of attack, applying the Kutta-Joukowski theorem we see that the coefficient of lift can be approximated by Eq. 12:

$$c_l = \frac{L'}{q_\infty c}; \quad \text{where: } q_\infty = \frac{1}{2} \rho_\infty U_\infty^2 \quad (12)$$

giving us a solution for the flat plate of $c_l = 2\pi\alpha$, where α is angle of attack.¹¹ Thus the result in Eq. 12 states that coefficient of lift is linearly proportional to the angle of attack. However, this approximation is more appropriate for an infinite span wing. Since in our experiment all the models have an aspect ratio of 2, we must take into account finite wings and low aspect ratio effects.

1.d. Prandtl's Classical Lifting-Line Theorem

For the finite wing effects, we first discuss Prandtl's classic lifting line theory. If multiple horseshoe vortices are bound to a single line, called the lifting line at different lengths along that line, the result is the circulation that varies along the line of the bound vortices. Since for a real wing, a pair of single vortices equidistant from the root is represented by a single horseshoe vortex, the strength of each trailing vortex is equal to the change in circulation along the lifting line.¹²

If we consider an infinitesimally small segment of the lifting line dy , with a change in circulation $d\Gamma$ along that segment, then an induced velocity dw is generated at point y_0 as shown in the Figure 4,¹³

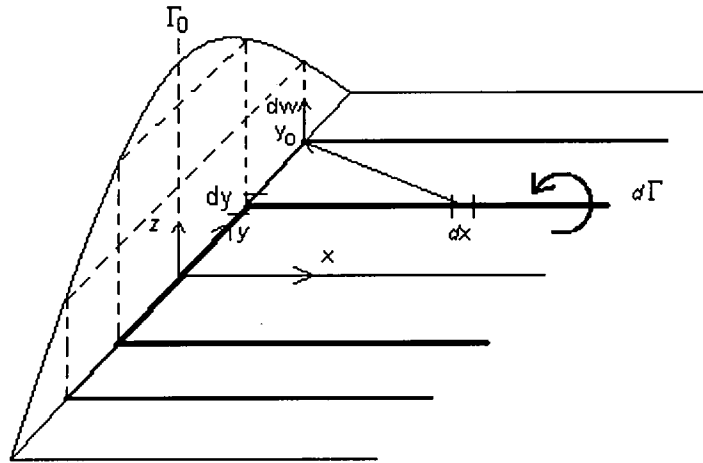


Figure 4: Superposition of vortices on the lifting line

and can be represented by using the Biot-Savart law, which is a fundamental relation in the theory of inviscid incompressible flow, with the expression in Eq. 13:

$$dw = -\frac{(d\Gamma/dy)dy}{4\pi(y_0 - y)} \quad (13)$$

From the relationship in Eq. 13, we can see the induced velocity is only a function of circulation and distance away from each individual vortex. However, integrating Eq.13 to get the total induced velocity w at y_0 , due to the entire vortex sheet along the entire span, we get the following expression:

$$w(y_0) = -\frac{1}{4\pi} \int_{-b/2}^{b/2} \frac{(d\Gamma/dy)dy}{y_0 - y} \quad (14)$$

Finally, taking into account the relationship between circulation and lift presented earlier by Kutta-Joukowski theorem, and assuming that the induced velocity given above is small compared to the freestream velocity, the fundamental equation of Prandtl's lifting-line theory for a flat plate is given by Eq. 15:

$$\alpha(y_0) = \frac{\Gamma(y_0)}{\pi U_\infty c(y_0)} + \frac{1}{4\pi U_\infty} \int_{-b/2}^{b/2} \frac{(d\Gamma/dy)dy}{y_0 - y} \quad (15)$$

$\alpha_{\text{effective}} \qquad \alpha_{\text{induced}}$

This relationship states that the geometric angle of attack is equal to the sum of the effective angle of attack, given by the first part of the expression and the induced angle of attack, given by the last segment of the above formula. This is a very interesting result, because it states that the circulation is key to obtaining aerodynamic characteristics such as the coefficient of lift and drag for finite wings, assuming inviscid and incompressible flow with insignificant induced velocity.¹⁴

1.e. Coefficient of Lift Theoretical Approximations

In order to accurately predict the coefficient of lift for each model, due to differences in geometries, we have to use different approximations as stated earlier. We first take a look at the elliptical flat plate.

For the elliptical wing we make an assumption that there is an elliptical lift distribution, meaning that downwash is constant over the entire span. Thus, from the earlier discussion of the induced velocity, we relate the wing's aspect ratio, AR, to the induced angle of attack, α_i , given by Eq. 16:

$$\alpha_i = \frac{C_l}{\pi AR} \quad (16)$$

However, in order to approximate the coefficient of lift more accurately, we also need to take into account the effective angle of attack. For a flat finite plate, zero lift is at zero degrees angle of attack. Also, for a flat plate, the relationship between the change in the lift coefficient and the change in the difference between the effective and induced angles of attack are the same as the relationship between the coefficient of lift and angle of attack for an infinite wing, namely:

$$\frac{dC_l}{d(\alpha - \alpha_i)} = a_0 \quad (17)$$

Integrating this relationship and substituting the definition of the induced angle of attack for an elliptical distribution of lift into the above equation, and then differentiating the relationship again with respect to the effective angle of attack, we get the slope of the coefficient of lift versus angle of attack for elliptical wings, given by Eq. 18¹⁵:

$$\frac{dC_l}{d\alpha} = \frac{a_0}{1 + a_0 / \pi AR} \quad (18)$$

Assuming that for low angles of attack the slope is linear and a_0 for a flat plate infinite wing is given by 2π , the final result for the coefficient of lift approximation of an elliptical wing is given by Eq. 19:

$$C_l = \frac{2\pi}{1 + 2/AR} \alpha \quad (19)$$

In our case, where $AR = 2$, the approximation boils down to a simple relation as given by Eq. 20:

$$C_l = \pi\alpha \quad \text{where } \alpha \text{ is in Radians} \quad (20)$$

It is very interesting to see that the coefficient of lift versus angle of attack slope for a flat plate, finite, elliptical wing of $AR = 2$, is exactly half of the infinite wing approximation. Although this relationship holds for an elliptical wing, it is interesting to see what the derived relationships for delta or rectangular wings with low aspect ratio are.

For rectangular, low aspect ratio wings or for swept delta wings, the assumptions behind lifting-line theory are no longer appropriate to estimate induced velocity and therefore coefficient of lift based on angle of attack. Lifting-surface theory must be used to make such approximations. If we first consider parameters as given in Figure 5¹⁶ below,

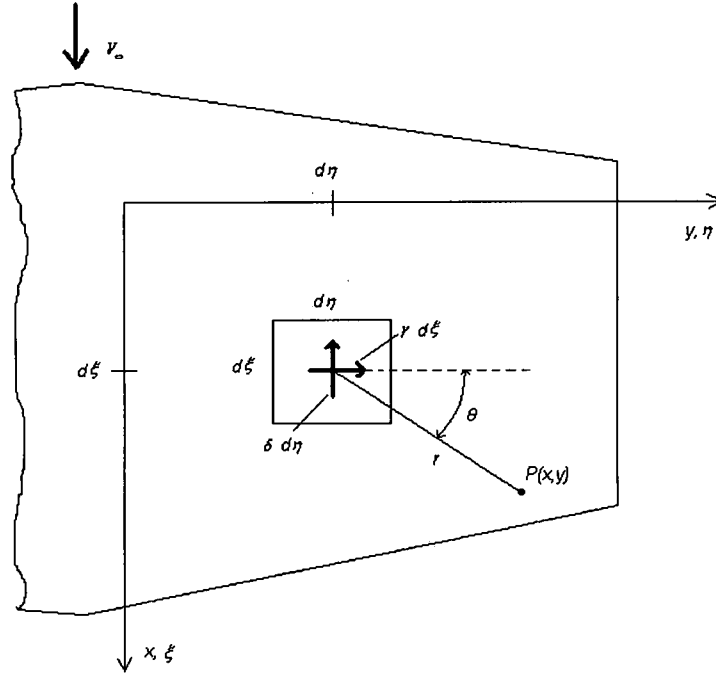


Figure 5: Induced velocity; Vortex lattice method

then the incremental velocity $|\mathbf{dV}|$, induced at point P by a segment $d\eta$ of a certain vortex filament of strength $\gamma d\xi$ that stretches in the y direction, can be given by Eq. 21¹⁷:

$$|\mathbf{dV}| = \left| \frac{\Gamma}{4\pi} \frac{\mathbf{dl} \times \mathbf{r}}{|\mathbf{r}|^3} \right| = \frac{\gamma d\xi (d\eta) r \sin \theta}{4\pi r^3} \quad (21)$$

Integration of the above equation to determine the induced velocity due to the entire vortex sheet for the whole wing, at least for rectangular low aspect ratio wings, produces a perhaps surprisingly simplified expression in Eq. 22¹⁸:

$$C_l = \frac{1}{2} \pi \alpha AR \quad (22)$$

The above equation is only true if we still satisfy Kutta-Joukowski condition by integrating up to a straight trailing edge. Also, Eq. 22 is valid only for wings with aspect ratios between 2 and 4, since below $AR = 2$, the wing behaves as a slender body and above $AR = 4$, the induced velocity can be approximated by easier expressions, such as Eq. 14. For the specific case of the wing having an aspect ratio of 2, assuming that Eq. 22 is still valid, the relationship between the angle of attack and the coefficient of lift can

once again be simplified to exactly the same formula as for the elliptical wing of the similar aspect ratio:

$$C_l = \pi\alpha \quad (23)$$

For a slender delta wing, the same assumptions as for the rectangular flat plate are difficult to make, since the flow is conical and similar in all transverse planes through the wing normal to the mainstream.¹⁹ Thus the integration of the fundamental equation is difficult. For delta wings, the lift distribution occurs in a triangular fashion, where the span is related to the sweep angle at local positions with x . The relationship between the angle of attack and the coefficient of lift is given by Eq. 24:

$$C_l = \frac{1}{2} \pi \alpha AR \left[\frac{4}{(2 + AR \tan \phi_{1/2c})} \right] \quad (24)$$

The relationship in Eq. 24 holds only for the assumption that $(AR \tan (\phi_{1/2c})) \geq 2$.²⁰ In our case, where the $\phi_{1/2c} = 45$ degrees, the quantity is equal to 2. Once again, in our exact case where the $AR = 2$, the above formula is simplified to:

$$C_l = \pi\alpha \quad (25)$$

This is very interesting, since it suggests that all three models should have the coefficient of lift versus angle of attack slopes equal to π , which is once again half of the slope for the infinite flat plate case.

Although these relationships between a coefficient of lift and angle of attack for the elliptical, the rectangular and the delta wings are predicted by classical fluid dynamic theories and once again are based on the inviscid flow assumptions, it is important to find out if the same relationships hold for viscosity-dominated low Reynolds number flows. Thus, the following chapter will discuss research, which has been performed at both high and low Reynolds numbers to study vortex generation and its effect on the coefficient of lift, and angle of attack relationship. Also, in the next chapter, studies which address viscous dissipation effects and vortex characteristics in low Reynolds number flows are discussed.

CHAPTER II

LITERATURE REVIEW

2.a. Real-world Application

The Federal Aviation Administration has created aircraft spacing guidelines for Air Traffic Control in an attempt to eliminate the risk of inadvertent flight of aircraft into the wake turbulence of the preceding aircraft. According to the Aeronautical Information Manual, vortex strength is dictated by the speed, weight and shape of the wing of the aircraft generating lift. The wing configuration of the vortex-generating aircraft also affects the strength of the wingtip vortex. The greatest strength occurs when the generating aircraft is heavy, in “clean” configuration (no flaps, slats or gear extended), and in relatively slow flight, such as during take-off or landing. Peak vortex tangential velocities as high as 300 feet per second have been recorded in the past.²¹

Numerous accidents have been attributed to flight into wake turbulence of the preceding heavier aircraft. Thus, the FAA has created minimum requirements for the air traffic wake turbulence separation of aircraft. Large aircraft operating behind other large aircraft at the same altitude are required to be separated by either 2 minutes and 4 miles from each other when taking off or by 4 miles only when operating in other phases of flight. For small aircraft operating behind large/heavy aircraft, the time extends to 3 minutes and separation distance increases to 5-6 miles depending on the vortex-generating aircraft. The Boeing B-757, for example, has its own category for separation requirements, stemming from the research done by NASA, due to the high strength vortices that the aircraft produces and the accidents that have been attributed to the vortices generated by this aircraft.²²

The wingtip vortices produced by aircraft dissipate proportionally with time. The vortices move spanwise outward along the bottom of the wing, up and over the wingtip

and cave back inwards. The wingtip vortices immediately following large aircraft are slightly less than the wingspan distance apart from each other. With time, due to ground proximity, the vortices move farther apart, sink downward at a decreasing rate or until they reach the ground, and decrease in circulation strength. However, this behavior of wingtip vortices has been studied closely almost exclusively for large-scale aircraft at high Reynolds numbers in the regions between 500,000 to 5,000,000, but has not been examined in detail for lower Reynolds numbers, in the regions of 1,000 to 25,000. Thus, in order to better understand and compare vortex roll-up behavior at low Reynolds numbers to the high Reynolds number regimes, this study will also focus on the relative position between the wing tip itself and the vortex core for different planforms, angles of attack and positions aft of the trailing edge.

There are only rare studies, either computational or experimental, that contribute to the understanding of the wingtip vortex generation and structure of the vortex velocity field based on basic parameters such as the angle of attack, planform and profile of the airfoil even at high Reynolds numbers in quasi-steady-state flows. There are even fewer studies that relate to the wingtip vortex understanding at lower Reynolds numbers.

2.b. Paper Review

In the recent experimental study written by Anderson and Lawton, a correlation between vortex strength and axial velocity in a trailing vortex was investigated.²³ In this experiment a NACA 0015 wing with a span of half the wind tunnel test section was placed into a flow regime with Reynolds numbers on the order of 750,000 to 1,250,000. Velocity flow fields were measured with a hot wire anemometer and axial velocity of the wing tip vortex core was correlated to the vortex circulation. As predicted by the Prandtl's lifting-line theory, the root circulation strength increased in direct proportion to the lift produced. At lower angles of attack, where less total lift is produced, the ratio of the axial velocity to the freestream velocity is less than or close to one. However, as the angle of attack is increased, thus increasing wing loading, the same ratio is increased beyond one with the maximum value being around 1.8. The correlation between circulation, which was normalized to the freestream velocity and wingspan, and axial-to-freestream velocity ratio, was investigated. The results show that for an increase in

normalized circulation the ratio of the axial-to-freestream velocity ratio grows linearly for Reynolds numbers of 1,250,000, 1,000,000 and 750,000.

$$\text{As } \frac{\Gamma}{U_{\infty} b} \uparrow, \quad \frac{u_x}{U_{\infty}} \uparrow \quad \text{linearly} \quad (26)$$

It is also evident from this experiment that the slope of this correlation and the axial velocity is greatest for a round tip of the wing at a distance greater than one chord length downstream of the trailing edge.

The Anderson and Lawton experiment, although closely related to this study, relates axial velocity to vortex circulation strength at relatively high Reynolds numbers and takes into account an airfoil with a thickness at half wingspan. However, whether the same correlation extends to flat plate wings of full span at lower Reynolds numbers at around 1,000 to 25,000 is still unknown. If the airfoil or a flat plate is placed into the flow where both ends of the wing are in the freestream, it is possible that circulation and axial velocity magnitudes will be lower even for the same Reynolds numbers, due to any possible wall effects or restricted spanwise flow velocity. Also, if this experiment is carried out at lower Reynolds numbers, the effects of the wing tip geometry on the strength of circulation and axial velocity might be different due to greater viscous dissipation effects at low Reynolds numbers. At least in theory, circulation from the vortex should be lower in low Reynolds number regimes than at high Reynolds numbers. Finally, the Anderson and Lawton experiment does not investigate variation of vortex flow field for different planform geometries.

A study performed by Martin V. Lowson attempts to look at the velocity field of the vortex sheet in the wake behind a delta wing.²⁴ The experiments were performed in a wind tunnel with a delta planform wing with a leading edge sweep angle of 70 degrees, a chord of 44.1 cm and thickness of 1.2 cm. Flow visualization was performed to quantify vortex sheet strength in a wind tunnel using pulsed laser and a 35 mm camera in the flow with freestream velocity that produced Reynolds numbers between 3,000 and 30,000.

Lowson suggests that in flows with Reynolds numbers below 6,600, viscous dissipation forces dominate to such an extent that the high Reynolds number theories for predicting vortex roll-up behavior and vortex strength break down. Lowson also suggests that high Reynolds number theories apply in predicting the behavior of the vortex core

and that low Reynolds number experiments can in some instances be used to predict the entire vortex sheet behavior to better understand full-scale model aerodynamic characteristics. Finally, Lowson argues that although there is some disagreement in the vortex roll-up behavior between theoretical high Reynolds number predictions and low Reynolds number experiments, the velocity distribution and vortex strength in the wake behind a delta wing at low Reynolds numbers are still consistent with the theoretical predictions for high Reynolds number flows.

This study describes the relationship between high Reynolds number theoretical vortex behavior and low Reynolds number experimental data for the delta planform wings, but makes no ties to other planforms, such as rectangular or elliptical wings. Also, although the range of chosen Reynolds numbers is consistent with the choice of Reynolds numbers in our study, Lowson's work doesn't compare the same parameters for different angles of attack, making it difficult to compare the overall circulation and coefficient of lift even for the delta wings of different sweep angles.

Another experiment on the near field structure of wing-tip vortex is written by S. Ah and S. Jung.²⁵ In their study a five-hole probe is used to measure the flow field of a vortex behind a NACA 6409 airfoil at 5 degrees angle of attack and a Reynolds number of 344,000. Once again, a semi-span model was used to produce wing-tip vortices.

The vortex structure was studied in the cross-flow plane and was found to have at least four distinct regions. The inner viscous core, that contains the maximum axial velocity, usually has an extremely small radius, that is hardly visible. The outer parts of the vortex consist of the "spiral out", "tightly wound spiral" and the potential vortex regions. As the vortex flows downstream, the flow pattern shows slight oscillation in vortex shape as well as each region radius. The explanation of these oscillations is believed to be the combined effect of the wing-tip vortex itself, and vortex sheet shedding along the wing tip and the trailing edge. Also, beyond one chord length downstream, only the inner and outer regions are present and it is almost impossible to distinguish between "spiral out" and "tightly wound spiral" regions. In this experiment, the axial velocity was also measured and found to be greater than the freestream velocity from the trailing edge to about one chord length downstream. Although maximum axial velocity is greater than the freestream velocity, the average axial velocity within the vortex core

region oscillates around the freestream velocity magnitude by around 10%. Finally, for the same flow regime, the tangential velocities were compared between the NACA 6409 and the NACA 23012, with the NACA 6409 having greater tangential velocity magnitude and thus stronger inner core vorticity (or circulation).

The last comparison clearly shows that airfoil profile has a direct effect on the structure and strength of the wing-tip vortex. Since camber will generally increase circulation strength, thus increasing the coefficient of lift versus angle of attack slope, this study will focus on a flat plate, with fixed thickness and no camber. Also, the higher Reynolds number in the Oh and Jung study does not provide any answers for the vortex structure at Reynolds numbers of 1,000 and 25,000 or addresses relationship between maximum lift coefficient and angle of attack as seen in Figure 1. Finally, there is no variation of angle of attack or planform geometries, at least two of which, as seen from the previous study, have direct impact on the strength of the axial velocity, circulation and ultimately coefficient of lift.

One of the few studies that attempt to look at the coefficient of lift and angle of attack relationship at low Reynolds numbers is the experimental work performed by E.V. Laitone.²⁶ In this study, rectangular planform wings were tested at Reynolds numbers near 20,000 and lift and drag measurements were taken using a force balance for flat and cambered plates in a wind tunnel. In this case, an aspect ratio of 6 was used for all the models, while specifically for rectangular flat plates, aspect ratios of 2.18, 4, 6 and 8 were used.

Laitone found that 5% camber of a rectangular flat plate with $AR = 6$ increases the maximum coefficient of lift from about 0.7 at 9 degrees angle of attack to around 0.95 at approximately 13 degrees. This shows that there is a clear advantage of cambered airfoil in order to produce lift at low Reynolds numbers near 20,000. It is also visible from the study that a 5% cambered airfoil also has the same advantage at higher Reynolds numbers near 42,000. The NACA 0012 was also placed into the flow with $Re = 20,700$ in both a conventional direction and with the sharp trailing edge pointed upstream. It was found that with the airfoil pointed in a reverse direction, with the trailing edge in front, the maximum coefficient of lift was increased by more than 30% from about 0.45 at 6 degrees AoA to nearly 0.67 at 10 degrees AoA. Rectangular flat

plate wing with an aspect ratio of 2.18, produced the coefficients of lift equal to 0, 0.31, 0.58 and 0.84 at 0, 5, 10 and 15 degrees angles of attack respectively, at $Re = 20,700$. These coefficients of lift, that were obtained from force balance measurements will be compared in Chapter VI, to determine if approximately the same values based on circulation calculations are obtained.

Although this study provides insight into the coefficient of lift and angle of attack relationship at low Reynolds numbers based on profile and camber, no experiments were performed to make the same correlation based on planform geometry. Also, since the measurements were performed in the wind tunnel at such low Reynolds numbers, with the lowest freestream velocity near 10 m/s, the accuracy of the measured lift force using a force balance with sensitivity of ± 0.01 g is questionable, even though the empty tunnel turbulence level was measured to be around 0.02%. Thus, the Laitone experiments are already at the limit of being able to measure forces at Reynolds numbers near 20,000 and do not attempt to look at the same parameters at Reynolds numbers less than 20,000. Finally, although Laitone addresses the coefficient of lift and angle of attack relationship at low Reynolds numbers based on force balance measurements, he makes no reference to circulation strength or trailing edge wing tip vortex generation and their relation to the coefficient of lift.

In one study relating to the near field dynamics of wing tip vortices published by Zuhail and Gharib, the vortices were produced by a NACA 0012 in a wind tunnel. As is the case in Anderson and Lawton experiment, the wing was a rectangular semi-span model mounted on one side of the test section such that the center of the trailing vortex off the end of a wing tip was created in the center of the test section. However, in the Zuhail and Gharib study, a stereo Particle Image Velocimetry system that allows for a three dimensional picture of the vortex formation and dissipation was used to understand the dynamics and structure of the trailing wing-tip vortex at Reynolds numbers close to 9,000. The most significant discovery of this experiment was the appearance of secondary vortices downstream of the trailing edge. In all cases, secondary vortices had the opposite sign, or direction of rotation, than the main center vortex. Also, at least one secondary vortex is significantly larger than the other secondary vortices, while still being less intense than the main vortex. The presence of the satellite vortices created

unsteady effects and fluctuations of the main wing-tip vortices. However, for a given angle of attack, there seemed to be no increase or decrease in radial fluctuation of the wing tip vortex center location with the change of downstream positions from the trailing edge. Also, for a certain position downstream of the wing tip, no decrease or increase in vortex center position fluctuation is found over a range of angles of attack.²⁷ This is very interesting, since the vortex is expected to move relative to the wing tip with position downstream of the trailing edge at least in high Reynolds number regimes and also should not be stationary relative to the wing tip at low Reynolds numbers.

Although the authors suggest that the unsteady motion of the wing-tip vortex is a result of an interaction between the main vortex and satellite vortices, any secondary flow would affect the dissipation process of the main vortex. However, the main question is the cause of the appearance of secondary vortices. Since measurements for this experiment were performed in the wind tunnel at such low Reynolds numbers, it is difficult to say with certainty that production of secondary vortices behind the wing tip was not at least in some part due to an unspecified in the study level of inherent wind tunnel turbulence intensity. The NACA 0012 is an airfoil with 12% thickness and was mounted to produce only one wing-tip vortex, not allowing for a closer understanding of the potential wake origins, as well as vortex structure or strength variation for different parameters such as planform geometry at certain angles of attack for a simple flat plate.

It is important to understand wing tip vortex effects that are produced by aircraft. Most studies performed to contribute to this understanding result from a desire to reduce the unwanted effects of wake turbulence behind large aircraft. However, the velocity structure of a wing-tip vortex is extremely complex and in order to understand its formation and dissipation origins, a closer look needs to be taken at less complex airfoil profiles such as flat plates. Also, nearly all studies that have been done on this subject have used either delta or rectangular planform cambered airfoils, making it difficult to isolate individual contributions of planform geometrical pattern to wing-tip vortex behavior and the extent of contribution to vortex generation due to camber. Even so, it is of interest to see if the same results, such as the increase in wing tip vortex intensity with the increase of angle of attack discussed earlier, can be extended to low Reynolds number flow regimes on the order of 1,000 - 25,000. So far, the small body of experimental work

that has been done to understand low Reynolds number wing-tip vortex velocity structure has been performed mostly on a qualitative scale. Experiments with flow visualization, vortex velocity field generalizations and unsteady vortex behavior provide many clues, but no answers to the true nature of the trailing edge wing-tip vortices at low Reynolds numbers. Also, experiments that have been performed in these flow regimes do not attempt to parametrically isolate possible effects of other important variables, such as planform geometry on non-complex structures like flat plates before advancing onto cambered airfoils. This thesis will focus on identifying quasi-steady-state variations in the characteristics of a wing tip vortex structure with alteration of wing planform geometry and angle of attack of a flat plate at Reynolds numbers on the order of 1,000 and 25,000 using a PIV system.

2.c. Expected Relationships Between Theory and Experimental Data

Since in our case kinematic viscosity is increased compared to most studies described earlier, both the vortex core radius and circulation are expected to decrease in magnitude. Also, because low Reynolds number flows are dominated by viscous effects, it is important to investigate if the same, high Reynolds number theories discussed in Chapter I, can be applied to low Reynolds number regimes.

Since viscous forces dominate in our case, it is expected that the vortex will dissipate much faster in low Reynolds number flows than in the high Reynolds number regimes. This may have some negative effects on the stability of the overall circulation calculations making it difficult to select the optimum distance downstream of the trailing edge to effectively and representatively calculate the coefficient of lift, based on the circulation and compare it to the theories discussed earlier. Although, as proposed by the earlier theories, where inviscid flow assumptions are made, Reynolds number was not taken into account to calculate the coefficient of lift, thus opening up a possibility that the same relationships between the coefficient of lift and angle of attack will hold for all three planforms.

In addition, it will be interesting to see the vortex roll-up behavior as a function of distance downstream of the trailing edge. It is expected that the vortices will slowly dissipate while moving downward and away from the wing root after being sucked up

into the low-pressure region. At high Reynolds numbers, at least near the walls, this is certainly the case, but for our low Reynolds number flow, this may be different.

Thus the wing tip vortex is parametrically studied by gathering experimental data to investigate the core vortex strength and the velocity structure of vortices in relation to the angle of attack, model planform shape, and the position of the vortex in the yz plane, aft of the trailing edge. The following 3 chapters discuss the methods used to obtain experimental data to compare between the coefficient of lift and angle of attack relationship based on theories derived in Chapter I, and that obtained from circulation calculations from digital particle image velocimetry.

CHAPTER III

DIGITAL PARTICLE IMAGE VELOCIMETRY

3.a. Components and Set-up

The two-dimensional digital particle image velocimetry (DPIV) technique is used in this study to measure the strength and structure of a wingtip vortex downstream of the flat plate models. The technique utilizes five main components: a high-power laser, optics, a test section properly seeded with particles, a digital camera and a computer with a frame grabber and software to process the images from the camera as seen in Figure 6.

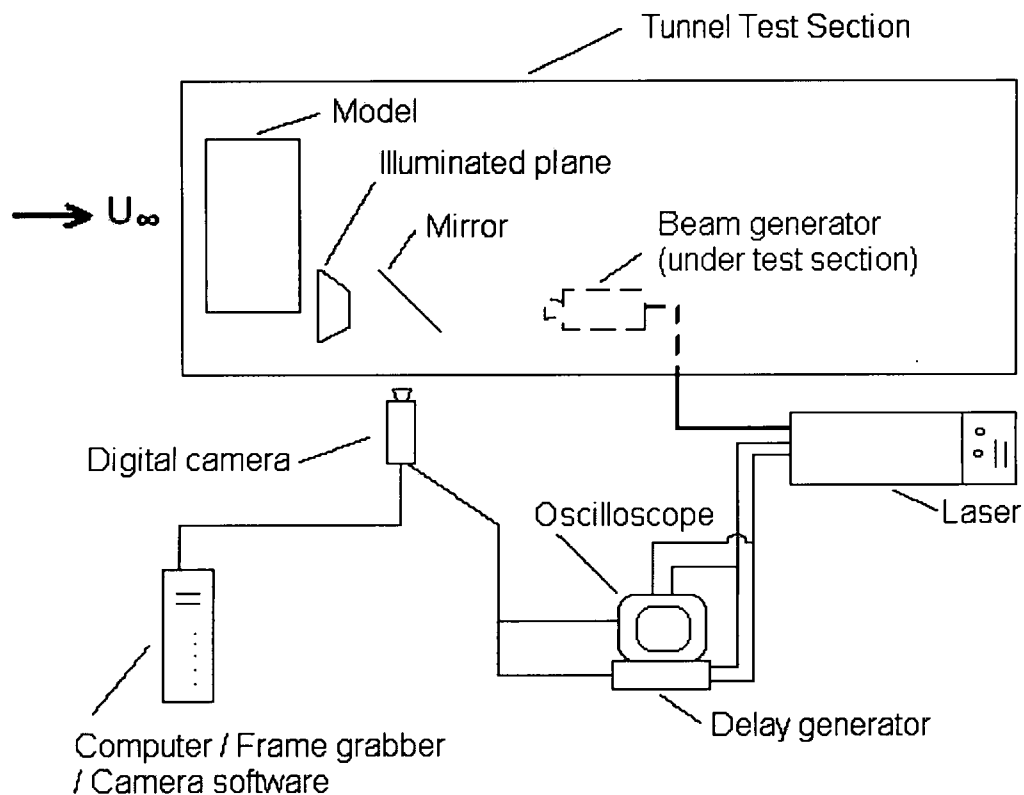


Figure 6: DPIV Set-up

All components must work together in synchronization to produce accurate results of the flow in the targeted plane. Therefore, this synchronization also requires a delay generator and an oscilloscope in order to verify the synchronization of the camera shots with the laser's flash lamps or vice versa. In this case the laser is synchronized with the camera that takes pictures at a frequency of 30 Hz. The laser has two flash lamps that fire independently and illuminate the targeted plane at the same frequency as the camera takes pictures, requiring each flash lamp to fire at 15 Hz.

3.b. Timing and Theory

The synchronization scheme is shown in Figure 7.

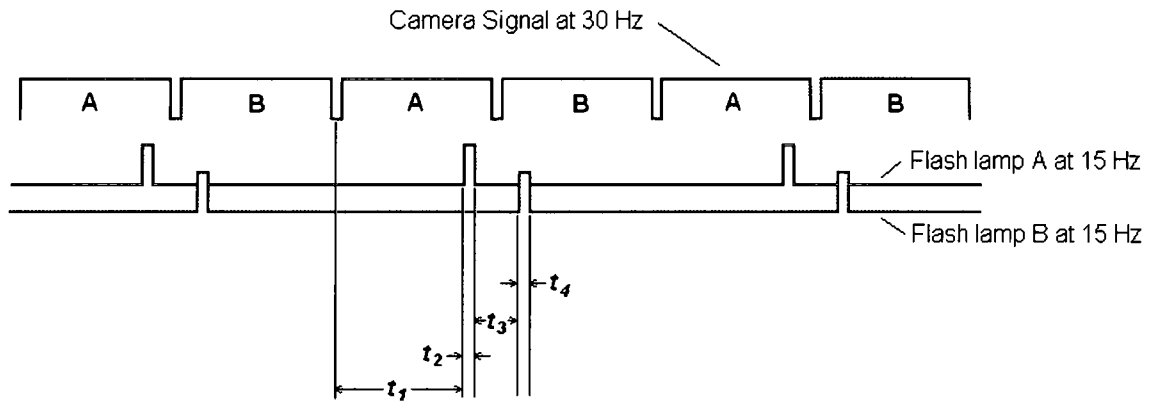


Figure 7: DPIV timing scheme

The time t_1 is on the order of 33000 μs , representing the timing of the first flash lamp firing from the instant frame A began capturing the image, as signaled by the camera. Times t_2 and t_4 represent the delay needed for the flash lamps to fire, about 110 μs . These times also translate to the amount of light that the frame can collect, increasing particle size as the times are increased, due to the prolonged exposure. These times are on the order of 300 – 500 μs , depending on the laser intensity and the required particle size. Finally, the sum of times t_2 and t_3 represents the actual Δt that is later used to calculate the in-plane velocity components. The greater the in-plane velocity, the smaller the time Δt required to obtain the results. Thus, the actual order of magnitude varies greatly depending on the application. Since we are concerned with obtaining the velocity components that are perpendicular to the flow, in this study a large Δt is required to capture enough displacement of particles in the plane of interest. It is important to note

that the sum of t_1 and t_2 , must be less than 33333 μs , and the sum of t_1 , t_2 and t_3 must be greater than 33333 μs for proper synchronization, because the camera takes pictures at a frequency of 30 Hz. The last requirement that must be adhered to, is that the sum of all times must be less than 66666 μs , in order for the first image pair, A and B, not to interfere with the second and so on.

As the laser illuminates the plane of interest, the particles that are seeded in the flow are recorded using the digital camera in frame A. After a time Δt , particles are recorded in frame B and the two frames are saved as an image pair AB. In this implementation of the PIV technique the image pairs AB are stored onto the RAM memory of the computer and later saved onto the hard drive as files in the .RAW format. Considering an image pair AB, where:

$$A = f(y, z) \quad \text{and} \quad B = g(y, z) \quad (27)$$

then in theory, the cross-correlation of the two images is represented by:

$$f(y, z) * g(y, z) = \int_{-\infty}^{\infty} \int_{-\infty}^{\infty} f(y + y_o, z + z_o) * g(y, z) dy_o dz_o \quad (28)$$

Basically, the image pairs are divided into smaller regions and the particles in the smaller regions are compared between the A and the B images to extrapolate local in-plane displacements. Since the time Δt between the images is also known, the velocity components can also be calculated.²⁸

CHAPTER IV

EMPLOYED METHODS

4.a. Camera Mounted Aft

The easiest place for the camera mounting, in order to investigate the wingtip trailing vortex in a cross-flow plane, is at first glance in the back of the water tunnel, looking through the window straight at the plane of interest as seen in Figure 8.

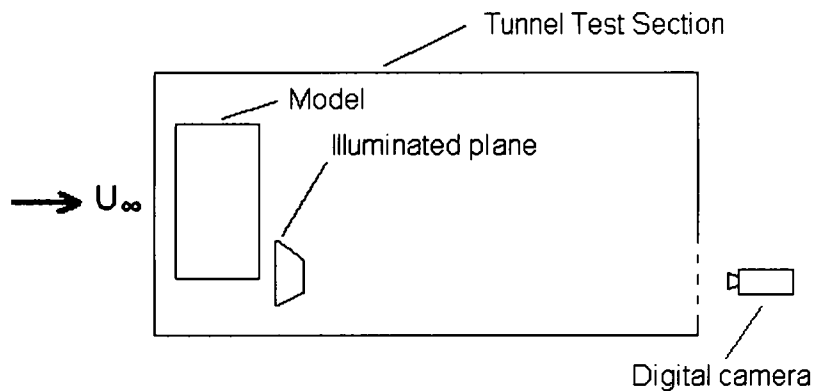


Figure 8: Camera behind a window at the end of the tunnel

However, diffusion and possibly refraction of the light traveling from the illuminated plane to the camera lens, positioned in the back of the tunnel, leads to astigmatism of the image as can be seen in Figure 9.

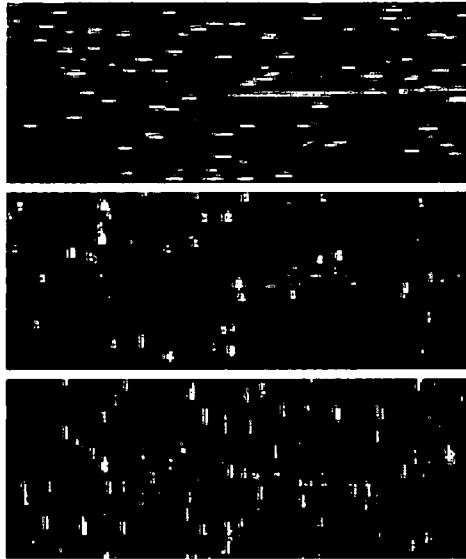


Figure 9: Astigmatism with camera in the back

In the above cases, the camera was mounted on the tripod looking in the direction opposite to the freestream velocity through the back window of the water tunnel. The difference between the three images is focal length of the camera lens. In all three cases, due to astigmatism, the image can either be focused in the horizontal or in the vertical plane. Even with the most symmetrical focus (with less apparent astigmatism), all the particles in the image appear at least 15 pixels in size. This case is unacceptable when trying to correlate between the images in a pair, since the ideal particle size for DPIV is about 3-5 pixels in the frame of 1024 X 1030. Changing the camera lens from 35 mm to 105 mm, yielded the same results. The images are still out of focus and the particle apparent size is still unacceptable. Thus, the actual diffusion or refraction from other particles in the path of the light, due to long travel through water from the plane of illumination to the camera lens, creates a physical limit to the distance at which the camera can be placed from the plane of interest. This problem is more prominent in water than in air and in our case is evident with 5 m of water between the plane and the lens.

The option of mounting the model 4 m downstream of the original position in the test section was investigated. However, the boundary layer effects at low freestream speeds of about 10 cm/s are significant enough to adversely affect the flow, rendering results unreliable. For example, using the Blasius flat plate approximation for the

boundary layer in the water at speeds of 10 cm/s produces a boundary layer 3.48 cm thick on all three solid sides of the open water tunnel test section after a distance of 4 m downstream. Such a thick boundary layer will account for more than 12% of the test cross-section area.

4.b. Viewing Through a Prism

In order to correct the astigmatism problem and shorten the distance that light travels between the plane of interest and the camera lens, an attempt was made to mount the camera about 30 cm past the trailing edge of the models. In this arrangement, the camera is looking at the illuminated plane through the glass at a 45-degree angle as seen in Figure 10.

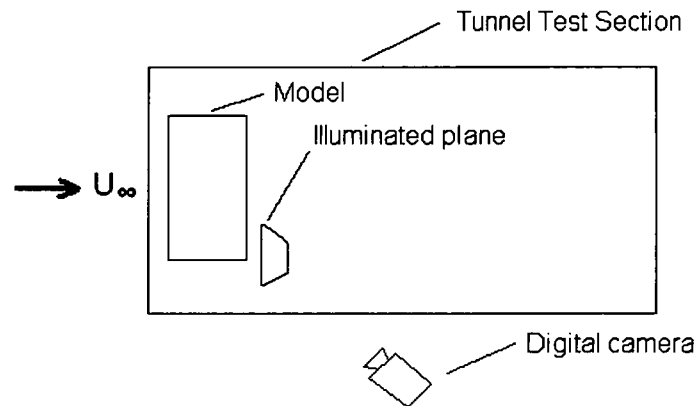


Figure 10: Camera mounted at 45 degrees to the plane of interest

This set-up creates two separate problems. The first problem is the refraction caused by the water to glass and glass to air surfaces. This refraction problem can be corrected using a prism large enough to have one face cover the entire lens of the camera and the other face of the prism placed flush with the glass of the tunnel test section. The exact angle of the prism in our case would have to be 38.3 degrees and the size of the prism for our purposes would have to be at least 6X6 cm. To order the prism would cost more than \$500 and the delivery time would have been more than 8 weeks, making this solution impractical.

The second problem is due to the different focal lengths that would be present when looking at a plane of interest at an angle. Basically, the particles in the image would not be focused well enough or uniformly enough for the cross-correlation software

to neglect the differences in apparent size of the particles. This creates a similar problem for cross-correlation as the astigmatism, but only for parts of the image. Once again, the apparent size of the particles is unacceptable and the undesired effect is more pronounced with a 105 mm than with a 35 mm camera lens due to the narrower depth of field. The problem can be solved using Scheimpflug rule, where a lens is placed at an angle between the plane of focus (in this case the illuminated plane) and the charge coupled device (CCD) chip. This requires a carefully crafted dark box, which enables the placement of the camera lens in such a way, that the illuminated plane, the camera lens plane and the CCD plane, all intersect along a single line, to correct the focus problem.

Solving the refraction problem and constructing the box to take advantage of the Scheimpflug rule, the set-up would look as shown in Figure 11

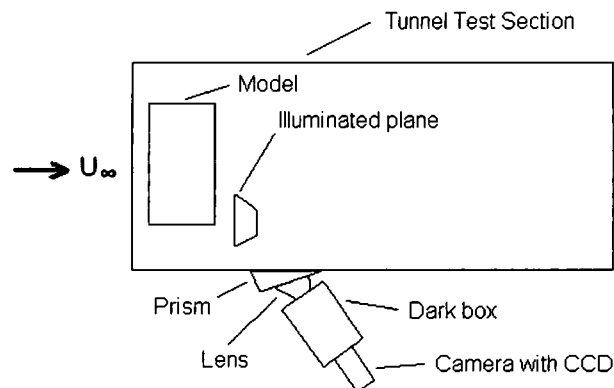


Figure 11: Camera at an angle to the plane of interest set-up

However, the price and delivery time for the prism, as well as the mounting challenges of the prism, camera lens, dark box, and the camera itself make this option impractical to get reliable results for using the DPIV technique.

4.c. Mirror Application

The actual method that was employed to obtain the DPIV results was placing the mirror inside the test section about 0.7 m downstream of the trailing edge of the model and turned at a 45-degree angle to the illuminated plane. The camera was focused through the mirror and was placed perpendicular to the test section glass from the side, as shown in Figure 12.

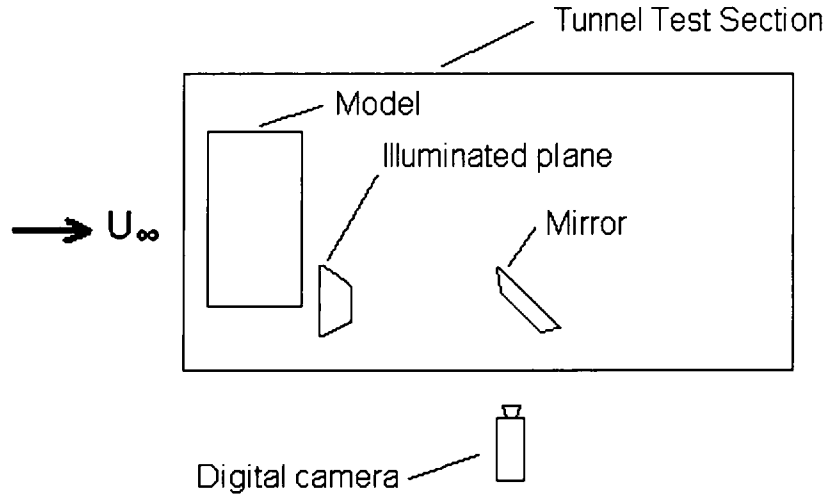


Figure 12: PIV set-up using the mirror

This set-up solves the astigmatism problem without complicating the system with refractive errors and eliminating the problems with the depth of view, since the camera is effectively focused perpendicular to the plane of interest. A sample resulting image from using this method is shown in Figure 13.



Figure 13: Rectangular wing; 10 deg. AoA; downstream $X/C = 1/10$; $U_\infty = 9$ cm/s; $Re = 8,028$;

The blockage effects of the mirror being submerged into the water are minimal. The wetted area that is exposed to the flow, when the mirror is turned at 45 degrees, is approximately 0.01 m^2 . With the test cross-section area equal to 0.28 m^2 and the mirror being placed more than 0.7 m downstream of the laser sheet, blockage effects, as they are related to the vortex velocity field, are insignificant with the mirror accounting for less than 4% of the cross-section area.

The only inconvenience with this method is that the z -coordinate is correct, as seen in the images, but the y -coordinate is reversed, where the wing tip and direction of circulation are observed to be in the opposite direction from actual, as viewed from any location downstream. Since all three models used in this study are symmetrical and both wing tips are equidistant from the walls of the test section, this problem can be solved by assuming that the images show the right wing tip, as opposed to the left, of which the shot is actually taken. However, in order get correct values for the circulation, equations were written to flip the models over and establish a coordinate system as seen in Figure 14.

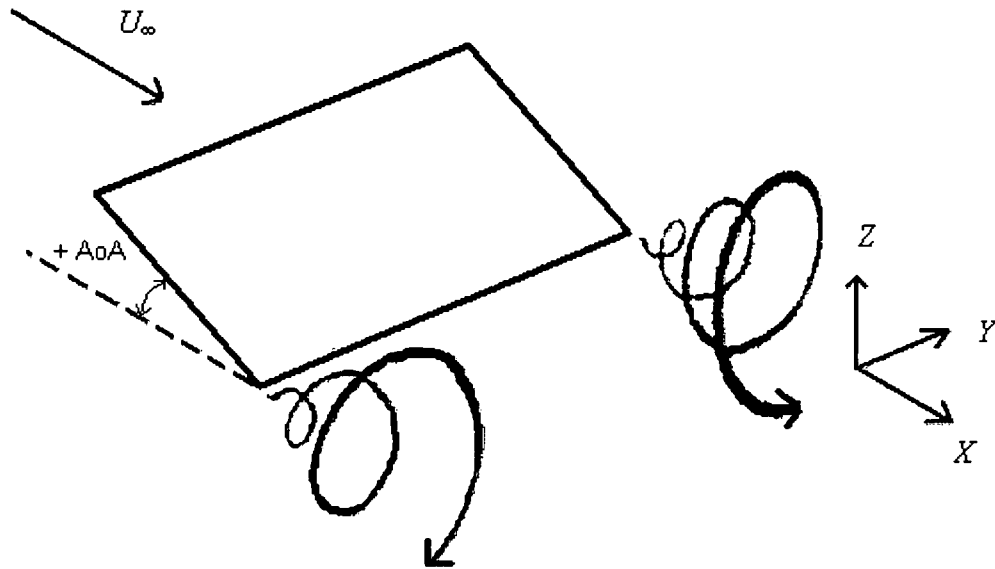


Figure 14: Coordinate System

4.e. Coordinate System

Due to the nature of water tunnel testing and the sting mount used in these experiments, all tests were performed with models placed in the flow at negative angles

of attack. Thus when referring to the angle of attack in positive magnitudes, such as 10 degrees, the model is actually submerged in the water with the same magnitude, but in the opposite direction (aka. -10 degrees). This convention later plays a role in how the vortex center position is related to the wing tip and the direction of the vortex roll-up.

Also, the use of the mirror, in obtaining the images for the DPIV, reverses the y -direction. However, since the models are symmetrical in the axis parallel to the freestream and are placed in the center of the test section, the test section wall effects, if any exist, between both ends of the wings are equal in magnitude. Thus, the problem of y -direction reversal is solved by flipping the model over, so that the top becomes the bottom. This is done in such a way so that there is no confusion if later tests are performed on cambered wings. The use of the mirror however, does not reverse the z -direction of the images and thus doesn't need to be corrected.

Thus, to correct for both the mirror y -direction reversal and models being placed at negative angles of attack problems, after the images are processed, they are inverted so that the position of the vortex relative to the wing tip and thus the model is presented in a conventional manner, as shown in Figure 14. This coordinate system was used for all quantitative results and analysis.

4.d. Flow Visualization

Flow visualization or dye injection was used to get some preliminary qualitative results to see the formation of the vortex, its strength over different positions downstream of the trailing edge, to get some idea of maximum velocity in the cross-flow plane and for the approximate placement of the mirror and camera to fit the entire vortex into the images. During the flow visualization trials the pressure in the dye system was brought up to 20 psi using an air compressor. The flow of the dye was regulated via the valves located near the dye reservoir, to make sure that the dye was flowing up to the test section and then through the flow control valves located at the top of the test section. Most complications were due to the dried up and clogged regions of the dye system, which necessitated higher initial pressure in the dye system to clear the flow channels. The system was initially brought up to 35 psi to clear the clogs.

Since the models are at a negative angle of attack in the water tunnel, the dye was injected on the higher-pressure surface of the models, as seen in Figure 15. The flow visualization images were later inverted to correspond to the conventional coordinate system shown in Figure 14. The vortices shed off the dye tube are not in the frame of the DPIV images and thus do not make any contribution to the calculation of circulation.

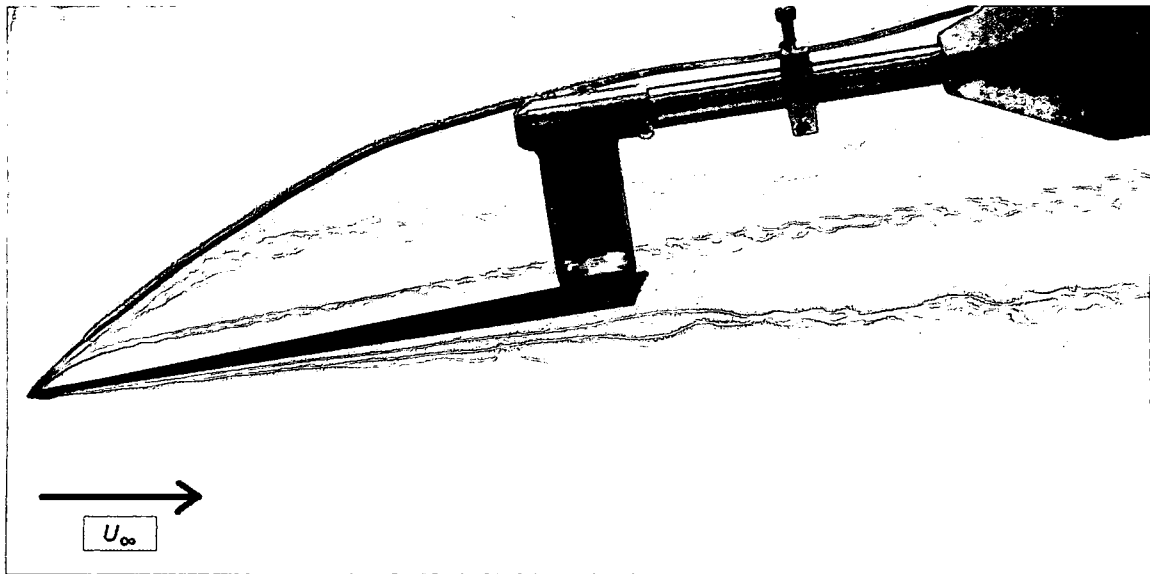


Figure 15: True orientation of the models

For the rectangular wing the end of the dye tube was placed about 5 mm inboard from the wing tip and 15% of the chord upstream of the trailing edge on the upper, higher-pressure surface of the model. For the ellipse, the dye tube was placed closer to the wing tip in order to observe a substantial amount of circulation. For the delta wing, the dye tube was moved to the leading edge of the wing, right at the tip. This choice of the dye injection location allowed for the visualization of both leading edge and wing tip vortices. Before explaining the test procedures, we first briefly describe the facility and mention equipment used to perform DPIV data gathering.

CHAPTER V

TESTS AND ANALYSIS

5.a. Models

In the experiments, flat plate models were manufactured from 1.5 mm stainless steel and painted black in order to minimize the glare from the laser beam. The model parameters and dimensions were chosen such that the mean aerodynamic chord, the span, the aspect ratio and the area for all three wings were the same. The only variable, was the planform geometry as seen in Figures 16, 17 and 18 below, representing the test models.

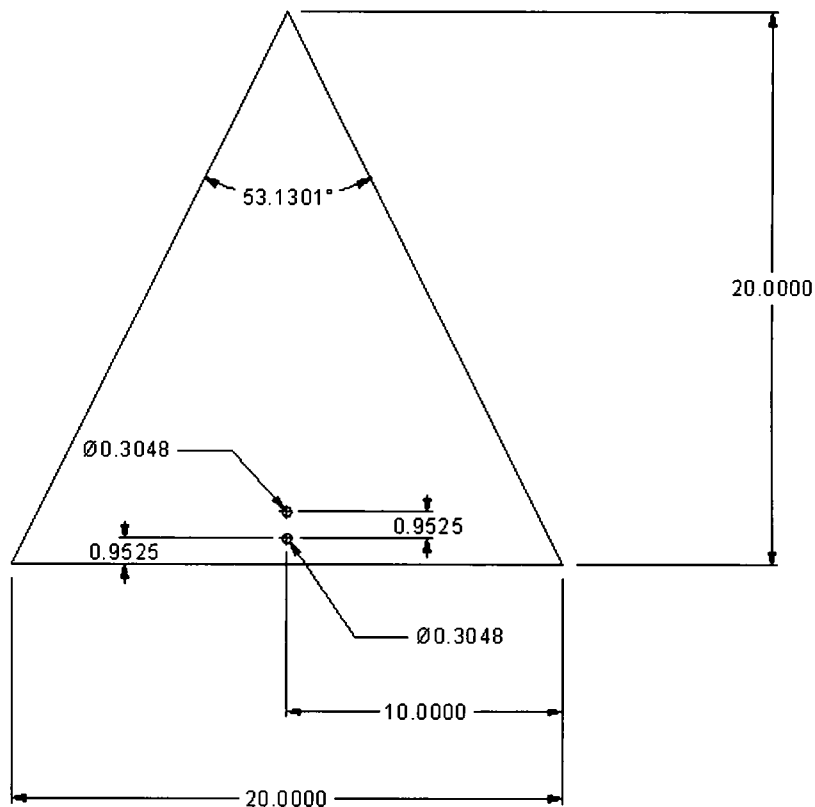


Figure 16: Delta wing; Dimensions in centimeters

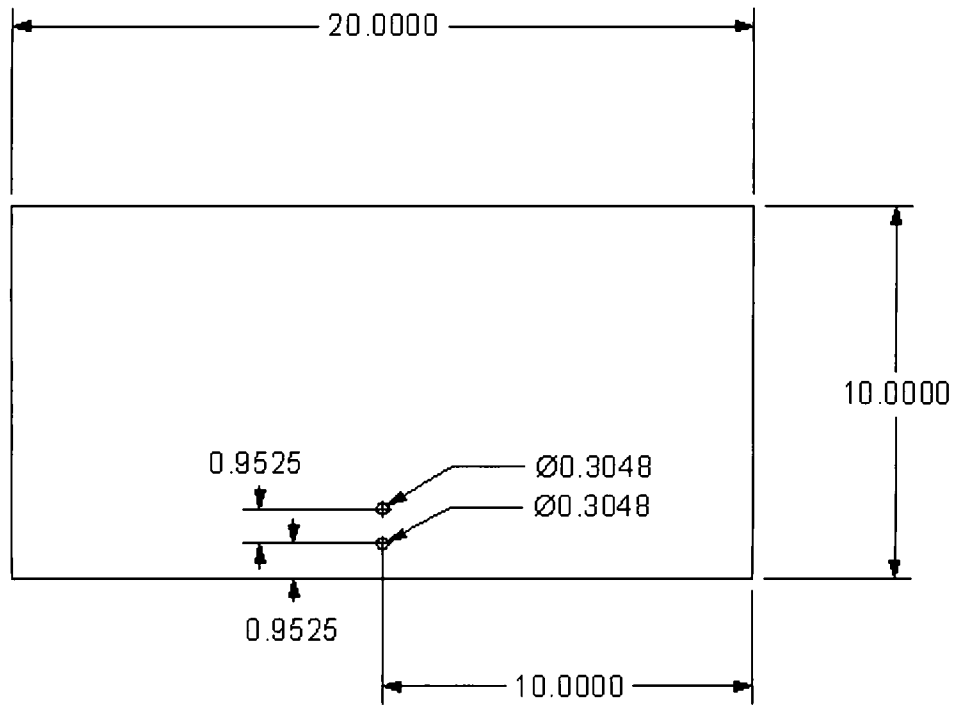


Figure 17: Rectangular wing; Dimensions in centimeters

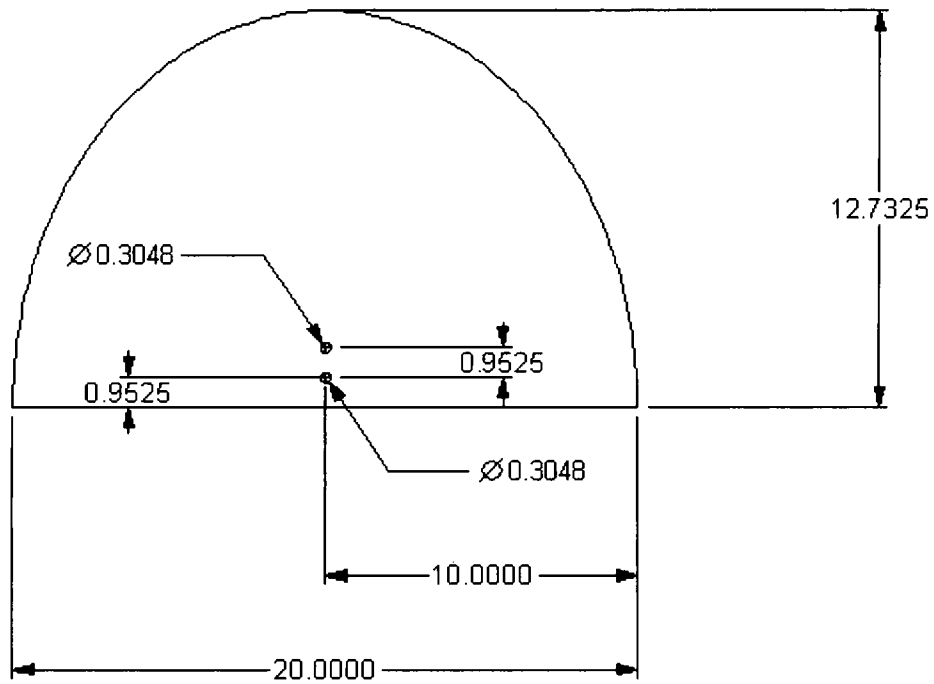


Figure 18: Elliptical wing; Dimensions in centimeters

water can also be filtered with a 1 hp recirculation pump, by passing it through a pair of paper filters. The particles used for the DPIV were TiO_2 (Titanium Dioxide) and were much smaller in diameter than the particles that were seeded in the water tunnel prior to this experiment. Thus, this filtration system had to be used to rid the water of the old particles and other impurities. The entire circuit is mounted on a structural steel framework.

The test section has $\frac{1}{2}$ in thick tempered glass on the bottom and sides, allowing maximum viewing of the models from the sides and the rear. However, to obtain usable DPIV data, only the sides were used as discussed in the earlier chapter. The centerline of the test section is 4 ft above the floor, which provides additional room under the test section to setup the DPIV equipment. From the pump, water flows through a perforated vertical 8 in diameter pipe at an upstream end of the intake plenum. Downstream of the delivery plenum, there are several flow-conditioning elements to eliminate unwanted flow turbulence. The contraction section area ratio is 4:1.

The camera that was used for taking the images was a UP-1830 Progressive Scan CCD Camera. It took images at a frame rate of 30 Hz and sent the command for laser pulse signals to the delay generator through a BNC cable. For flow visualization, a 20 mm camera lens was used, while for DPIV data gathering, 60 mm camera lens was employed. The image data was sent to the computer via a 10-bit RS-644/LVDS digital output connector cable.

To create a beam and illuminate the cross-flow plane of interest a New Wave Research "Minilase II" 50 mJ/pulse Nd:YAG laser and different optical components were used. The optics included an elliptical lens to constrain the width of the beam that comes out of the laser head, two semi-cylindrical lenses to flatten the circular beam nearly into a line and a mirror to redirect the beam up into the plane of interest. The laser has two flash lamps and is water-cooled. Distilled water circulates between hot, power-producing components. The timing scheme of the laser flash lamps is shown in Figure 7. When taking data, the laser was always operated on high power with power regulator set approximately between 225 and 270, to achieve desired illumination of the seeded particles.

5.c. Data Gathering

For the rectangular wing, the 20 mm camera lens was used to perform flow visualization. The model was submerged into the flow at 5, 10, 15 and 20 degrees angle of attack and the $U_{\infty} = 9$ cm/s, resulting in $Re = 8,028$. To perform flow visualization on the ellipse, the freestream velocity was also 9 cm/s with the model being submerged at 5 and 10 degrees angle of attack. In both the rectangular and elliptical wing tests, the dye tube was placed near the wing tip. Finally, for delta wing, the dye tube was placed at the apex of the wing, in the flow with $U_{\infty} = 9$ cm/s, and the model being at 10 and 15 degrees angle of attack. All the trials are tabulated in Table 1.

	$U_{\infty} = 9$ cm/s ($Re = 8,028$)			
	Angle of Attack			
Ellipse	5	10		
Rectangle	5	10	15	20
Delta		10	15	

Table 1: Flow visualization test matrix

After the approximate location of the vortex relative to the wing tip was determined with the help of flow visualization, digital particle image velocimetry was performed in order to enable calculation of the magnitude of the circulation. The models were mounted on a stainless steel sting via a T-type connector and two screws. The sting was easily moved in the stream-wise direction on the steel rails with the help of ball bearing wheels. To align the models correctly, every time a new model was installed, the first step was to make sure that the model is parallel to the test section bottom and had no bank. This was done with the help of a gravity leveler placed in the x and y directions. Once the model was level, the calibration wheel was moved to reflect the absolute zero angle of attack. The model was then rotated to reach the desired angle of attack and locked to make sure it didn't change throughout the test trial. Then, the model was lowered to the height of the camera, locked in the vertical axis and the trailing edge was aligned with the laser beam using the railings of the entire sting assembly. The entire assembly was locked using four nylon screws to make sure the model didn't move stream-wise. Finally, the micrometer was zeroed and then the model was moved to the predetermined position X/C upstream of the laser beam plane. Once the data was taken, a shot of a ruler in the plane of the laser beam was taken to determine spatial resolution.

The change in time Δt , between the laser flash-lamp pulses, which was set using a delay generator, for $U_\infty = 9$ cm/s was 5 ms, where Δt for $U_\infty = 27$ cm/s was reduced to 1.5 ms. The selection of these Δt 's, ensured that the bulk of all particles captured in image A are also present in image B, minimizing out-of-plane particle loss, as well as to stay within the Nyquist criterion limits for a 32 X 32 window during cross-correlation. The data was collected based on the test matrix shown in Table 2.

	$U_\infty = 0.09$ m/s (Re: 8028)			$U_\infty = 0.27$ m/s (Re: 24083)		
	X/C = 1/10	X/C = 1	X/C = 2	X/C = 1/10	X/C = 1	X/C = 2
Ellipse	AoA (deg)	AoA (deg)	AoA (deg)	AoA (deg)	AoA (deg)	AoA (deg)
	10	10	10	10	10	10
	15	15	---	15	15	---
Rectangle	5	5	5	5	5	5
	10	10	10	10	10	10
	15	15	---	15	15	---
Delta	10	10	---	10	10	---
	15	15	---	15	15	---

Table 2: DPIV test matrix

For each of the above 34 trials, more than 180 images were produced. This equates to 92 pairs of images for the delta wing, 93 image pairs for the rectangular flat plate and 92 pairs for the ellipse. The images that were stored on the computer, which communicated with the digital camera, were saved in a Photoshop format, .RAW. After the data was gathered over several weeks, it was transferred onto a personal computer, where post-processing and analysis were performed.

5.d. Post-processing and analysis

Data was processed using two different methods. The first method was used to obtain the results in the ISSI dPIV format to obtain accurate vortex center positions relative to the wing tips and also to obtain qualitative analysis and make observations regarding the vortex velocity and vorticity structures, and the overall stability of the vortices. The second method employed different algorithms that are used in obtaining quantitative results such as velocity and circulation. The output of the second method was viewed with the help of Tecplot software. Excel software was used to represent the

results of quantitative data such as vortex center position relative to the wing tip, velocity and circulation obtained from either method.

To process the images into a format that is compatible with the dPIV software, from ISSI Inc, the images were first processed in Photoshop and converted to .BMP format from .RAW. This was done using a macro that is built into Photoshop. Then, the .BMP images were all “batch-processed” or cross-correlated in one iteration using the correlation size of 32 pixels and 50% image overlap.

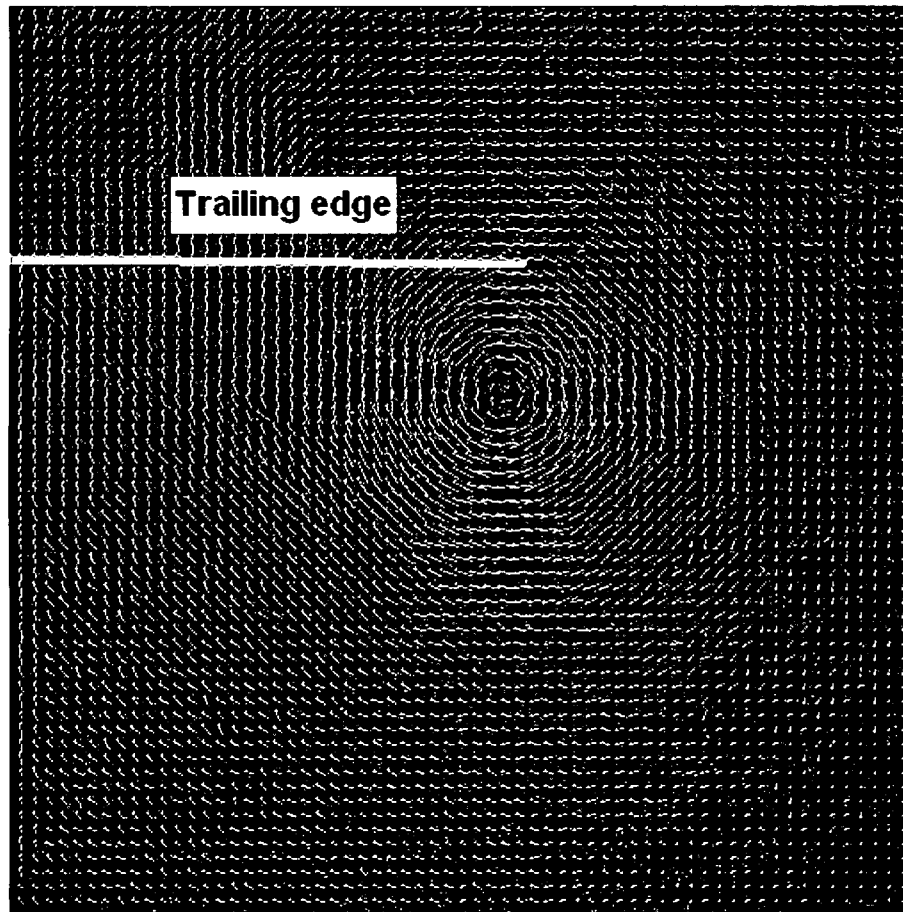


Figure 20: Rectangular wing; 10 deg. AoA; downstream $X/C = 1/10$; $U_\infty = 9$ cm/s; $Re = 8,028$; dPIV velocity vectors;

This procedure produces cross-correlated individual pairs, an example of which is shown in Figure 20. However, to get the average velocity and subsequently vorticity, for each trial, each pair (90+) was averaged. Knowing the resolution for each image, 13.228 pixels/mm, the velocity vector field was obtained. The final average velocity vector file

was then overlaid onto the trailing edge image and the number of pixels from the trailing edge to the vortex center was calculated as seen in Figure 21.

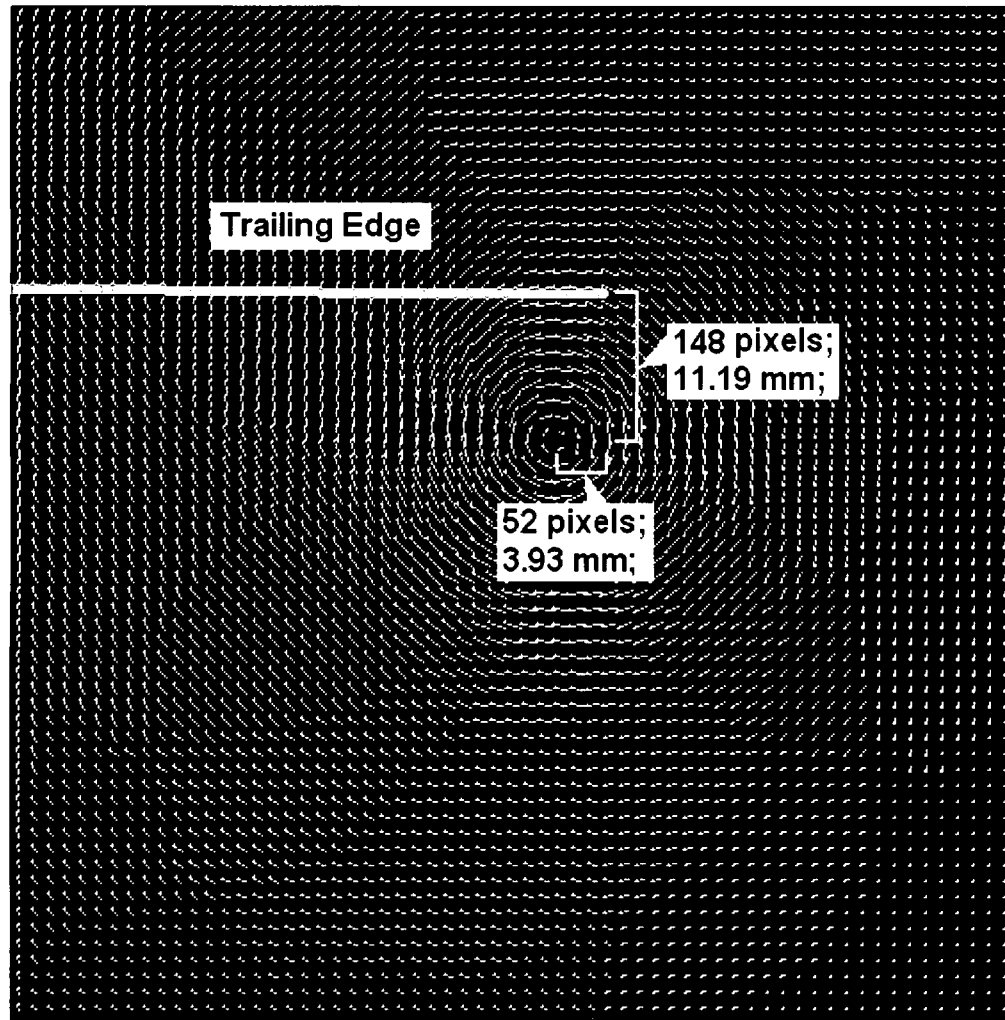


Figure 21: Rectangular wing; 10 deg. AoA; downstream $X/C = 1/10$; $U_\infty = 9$ cm/s; $Re = 8,028$; 93 image pairs average velocity and distances between vortex center and wing tip;

Each number of pixels was then calibrated to obtain relative distances between the wing tip and the vortex center. Since the only somewhat qualitative results obtained with this method were used to calculate the distance of the vortex center relative to the wing tip, it was not necessary to invert the images before performing analysis, as discussed in the previous subsection. Also, using dPIV software, excellent qualitative results were obtained in order to observe general vortex behavior. However, to obtain the average velocity vectors for calculating vorticity and circulation, and finally coefficient of lift, the second method of post-processing was implemented.

The second method implements image processing algorithms, provided by Dr. Michael Ol, which are fundamentally similar to those used by the dPIV software. However, to get more accurate results using the second method, the images first had to be processed in Photoshop in order to increase both the contrast and brightness. By processing the images first, the number of outliers seen in Figure 22, resulting from cross-correlating individual image pairs is reduced, which in turn, after averaging all the image pairs for each trial, increases the accuracy of the overall velocity vector field, resulting in more accurate circulation and coefficient of lift calculations.



Figure 22: Outliers for delta wing; 10 deg. AoA; downstream $X/C = 1/10$; $U_\infty = 27$ cm/s; $Re = 24,083$;

In order to increase the brightness and contrast of each image, a macro program was written, since manual processing would have been very lengthy and time-consuming. For delta wing results, the brightness and contrast were increased by 55%. However, for both the elliptical and rectangular, wings brightness and contrast were both increased by 35%. The increase in brightness and contrast virtually eliminated outliers. The images were then cross-correlated after being renamed. Using this method, calibration values of spatial and time resolution were defined for each case separately depending on freestream velocity and Δt before cross-correlation.

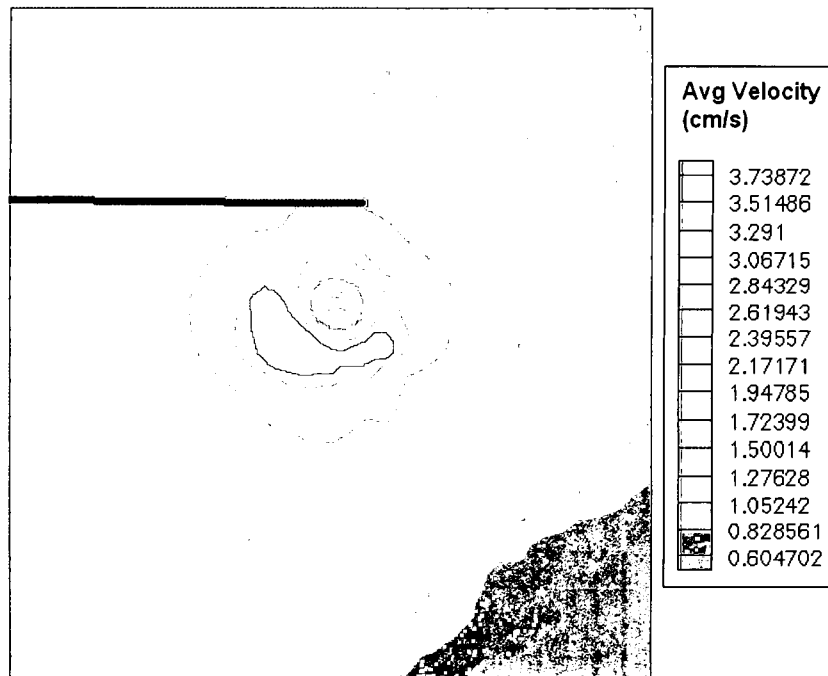


Figure 23: Rectangular wing; 10 deg. AoA; downstream $X/C = 1/10$; $U_{\infty} = 9$ cm/s; $Re = 8,028$;
Average velocity field;

In order to make sure vorticity and velocity field were presented in a conventional manner, as defined in Figure 14, vorticity images were inverted as seen in Figure 24.

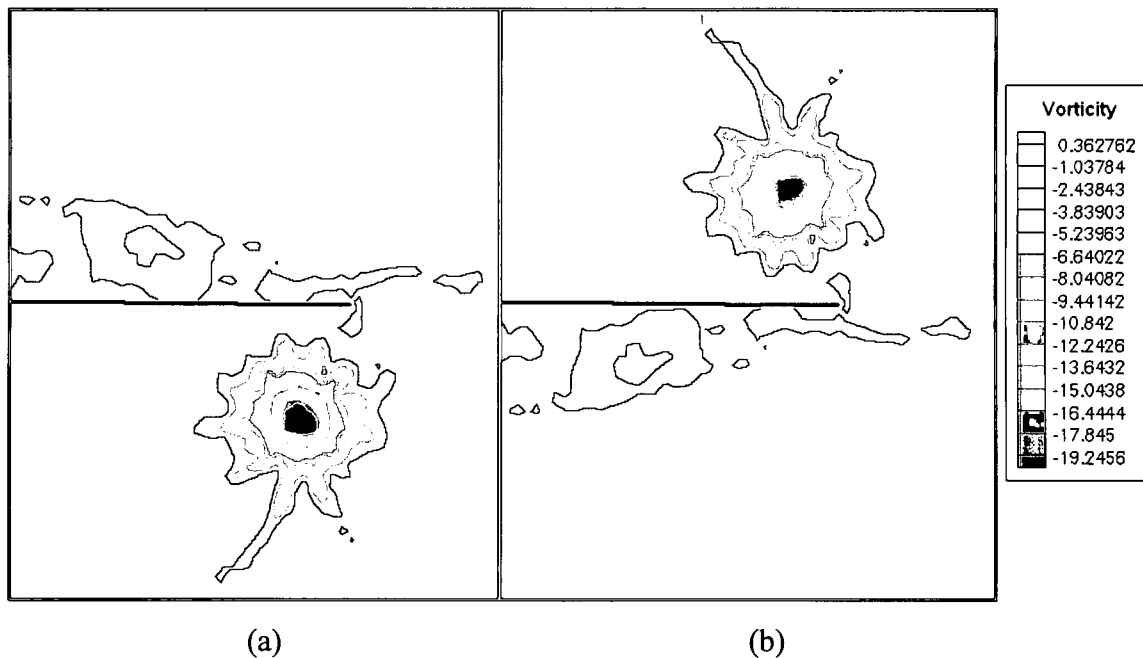


Figure 24: Rectangular wing; 10 deg. AoA; downstream $X/C = 1/10$; $U_{\infty} = 9$ cm/s; $Re = 8,028$;
a) Orientation as tested; b) Inverted vortex;

After cross-correlating the images, the approximate center for each vortex was obtained and the maximum absolute value of circulation for each trial was calculated as seen in Figure 25. Circulation was calculated using Eq. 8, where \mathbf{V} is the velocity field vector extracted from the DPIV results and $d\mathbf{s}$ represents the infinitesimal circumference distance on a closed circular curve C with a particular radius. The radius step size of 0.02 cm was used from the vortex center at 0 to a specified maximum radius. The maximum radius used for circulation calculations was 4.5 cm, in order to make sure that the entire vortex was included.

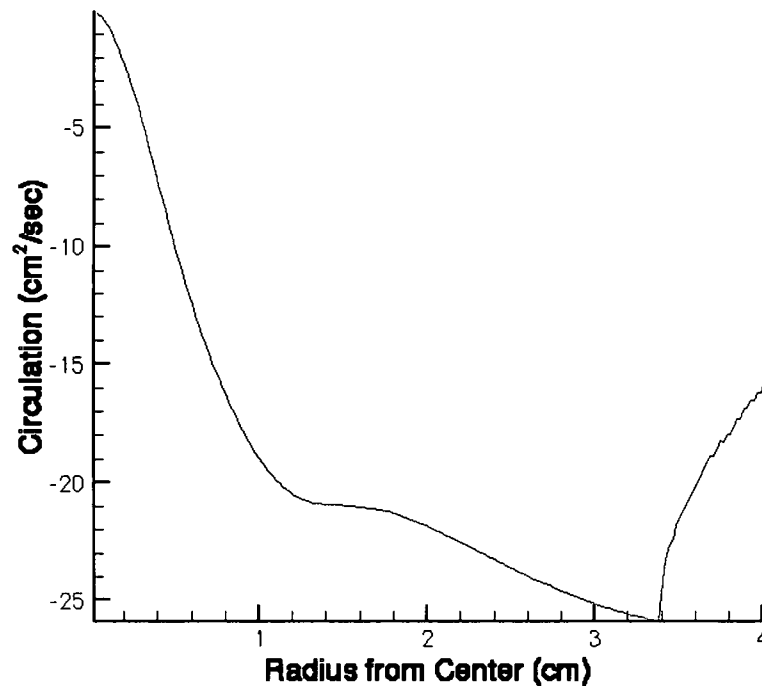


Figure 25: Rectangular wing; 10 deg. AoA; downstream $X/C = 1/10$; $U_\infty = 9$ cm/s; $Re = 8,028$; Circulation;

However, for about 90% of the trials, the maximum value of circulation was obtained at the radius value of less than 3.5 cm. Once all the data was post-processed, actual analysis and quantitative data comparison were performed using Excel.

Using the results obtained with DPIV software, relative distances between vortex center and wing tip were plotted as a simple Cartesian coordinate graph, with the origin being the wing tip. Although the images of the velocity vector fields were not inverted to represent the convention stated earlier in this chapter, it wasn't necessary, since the actual distances were easier to plot in the established convention rather than inverting the

images first, and then calculating the values for the distances. Thus, the graph is presented with the wings being oriented in the conventional manner as shown in Figure 14.

Other quantitative data such as the velocity vector field, the vorticity and the circulation were obtained and viewed with the help of Tecplot software. Once absolute circulation was calculated, Excel was used to normalize circulation to freestream velocity, U_∞ and mean aerodynamic chord, \bar{c} using the relationship:

$$\bar{\Gamma} = \Gamma / U_\infty \bar{c} \quad (29)$$

Also, lift and coefficient of lift obtained from experimental results were calculated using Excel with the following respective formulas:

$$L = \Gamma \rho_\infty U_\infty b \quad (30)$$

$$c_l = \frac{L}{q_\infty S} \quad \text{where: } q_\infty = \frac{1}{2} \rho_\infty U_\infty^2 \quad \text{and} \quad S = bc \quad (31)$$

Thus the comparison between theoretical values and experimental results as well as the apparent viscous dissipation effects for each trial were plotted using Excel software.

Using the techniques mentioned in this chapter, the results and conclusions are presented in the following sections

CHAPTER VI

RESULTS

6.a. Flow Visualization

As discussed earlier, flow visualization was performed on all three models to observe vortex flow behavior in the water tunnel. The most prominent difference in the flow around the models is the symmetry and structure of the vortex. The wing that produces the best-structured and most symmetrical vortex roll-up is the rectangular wing. As shown below, in Figure 26, the vortex sheds from the wing tip downstream of the trailing edge with a tangential velocity of approximately $1/3$ of the freestream velocity, which was determined based on known frame rate and approximate vortex roll-up distance.



Figure 26: Rectangular wing; 5 deg. AoA; $Re = 8,028$; Flow visualization;

We can also see that the vortex period does not change very much with distance downstream of the trailing edge and the distance between peaks is almost constant, suggesting that viscous dissipation effects are minimal at Reynolds numbers of approximately 8,000. It is also interesting to note that the vortex rolls upwards (into the low pressure region), which is different for the high Reynolds number flows, where vortex is shed downwards. This roll-up of the vortices upwards cannot be due to the presence of the sting in the flow, due to the sting's slender design. The proof of sting's minimal effects on the flow can be seen in Figure 27, where even the dye that is injected near the center of the delta model and thus flows closer to the sting, is not deflected upwards. Finally, although not visible in this picture, spanwise flow on the bottom of the rectangular wing is not significant, compared to the freestream velocity. Spanwise flow velocity component is less than approximately 10% of the freestream velocity, which was determined based on spanwise deflection of the dye when the tube was placed at the root of the model, where the least amount of spanwise flow is expected.

On the other hand, delta wing produces greater spanwise flow than a rectangular wing, starting from the apex of the model and moving outward from the root in nearly a straight line at approximately 16 degrees. The vortex that is seen in Figure 27 shows leading edge vortices shed from the apex of the delta wing with tangential velocity component being once again approximately 1/3 of the freestream velocity.

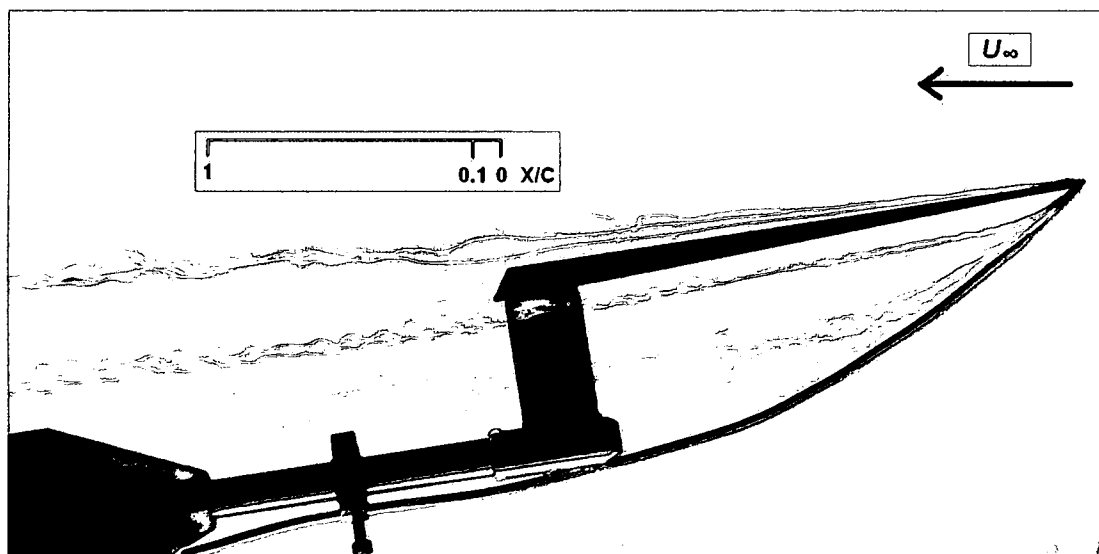


Figure 27: Delta wing; 10 deg. AoA; $Re = 8,028$; Flow visualization;

The structure of the vortices generated by the delta wing however, is less symmetrical than the structure of the vortices generated by the rectangular wing. This is clear from the picture where the roll-up of leading edge vortices is less pronounced and less stable. This suggests interactions between possible secondary vortices (not clearly visible) and/or greater viscous dissipation effects. However, since the Reynolds number is the same for the delta wing as for the rectangular flat plate and maximum tangential velocities are similar, viscous dissipation is probably still not significant. For the delta wing, unlike for the rectangular wing, the vortex rolls downwards, mimicking the behavior of vortices at high Reynolds numbers. The vortices at the bottom of the wing are most likely generated by the dye pipe, representing Karman vortex flow, and are not present in the DPIV results.

Finally, the least defined vortices are present in the flow around the elliptical wing. The flow is difficult to even qualitatively characterize and represents a large amount of interaction between primary wing tip vortex and the secondary vortices, shed off the leading edge. The tangential velocity component is approximately 1/4 of the freestream velocity since the peaks of vortices are farther apart from each other than for rectangular and delta wings as shown in Figure 28.

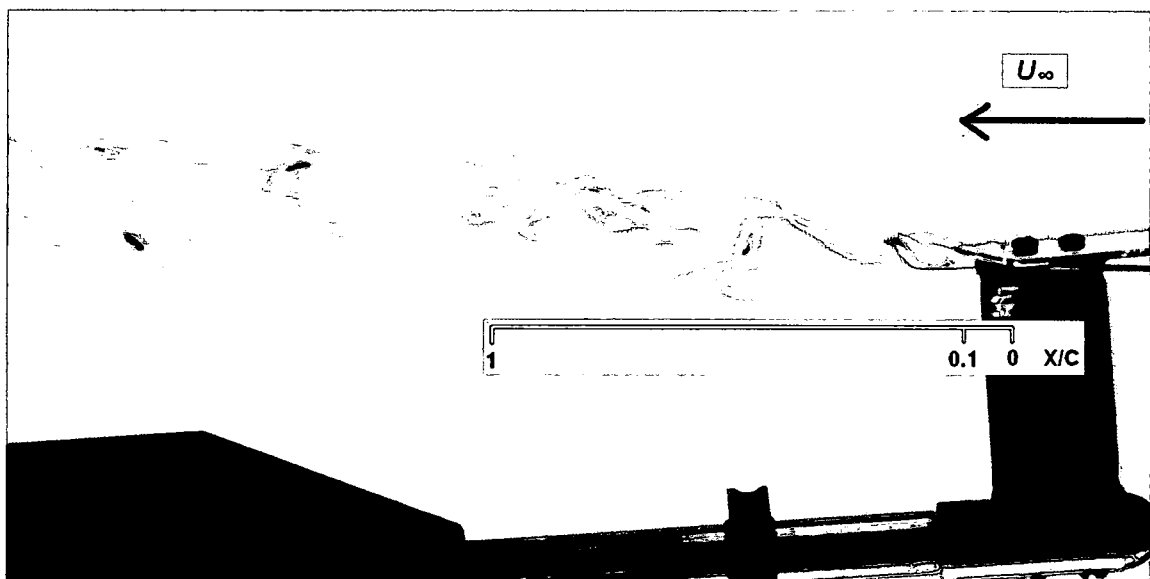


Figure 28: Elliptical wing; 5 deg. AoA; Re = 8,028; Flow visualization;

Complex, elliptical leading edge creates not only multiple secondary vortices, but also very significant spanwise flow, with the spanwise velocity component approximately equal to the freestream velocity. This is based on the observation that at the root of the ellipse, dye is deflected spanwise at nearly 45 degrees. The effects of viscous dissipation are greatly masked by the interaction between primary and secondary vortices and thus difficult to characterize. Behavior of the vortex roll-up past the ellipse is similar to the rectangular wing, where the vortex is drawn up into a low-pressure area behind the trailing edge, rather than for the delta flat plate, where the vortex dissipation once again mimics high Reynolds number flows. This disagreement in vortex roll-up behavior between the rectangular and elliptical wings, and the delta flat plate, cannot be due to the difference in the angle of attack, since for both the rectangle and the ellipse, vortex is still drawn upwards even at 10 degrees AoA.

It is interesting to note that for both the rectangular and elliptical wing planforms, vortices are first sucked into the apparent low-pressure region. This suggests that the models behave more like bluff bodies in the flow than slender bodies. However, the delta wing does not seem to mimic the same behavior, raising a question as to how planform geometry effects flow characteristics at low Reynolds numbers as they relate to lifting and bluff body classification. Finally, it is also interesting to note that the planform geometry that produces the greatest spanwise flow at low Reynolds numbers, which in our case is the ellipse, is also the shape that at least at high Reynolds numbers has the lowest lift induced drag coefficient.

6.b. Velocity and Vorticity Observations

As expected from the above flow visualization results, tangential velocity profiles for all three models are slightly different. After performing digital particle image velocimetry according to the test matrix discussed in Chapter V, the following observations can be made regarding the vortex velocity structure, vorticity and vortex roll-up behavior.

In general, all the quantitative results for the elliptical planform are less accurate than for delta wing, which, are in turn less accurate than for the rectangular flat plate.

These inaccuracies are mainly due to the instability of the vortex behind the trailing edge for the ellipse and delta, and also due to the greater interaction between secondary and primary vortices for these two models. Thus, averaging effects of the secondary vortices over more than 90 runs for each test, reduces the magnitude of the velocity field and decreases maximum vorticity values as can be seen in Figure 29.

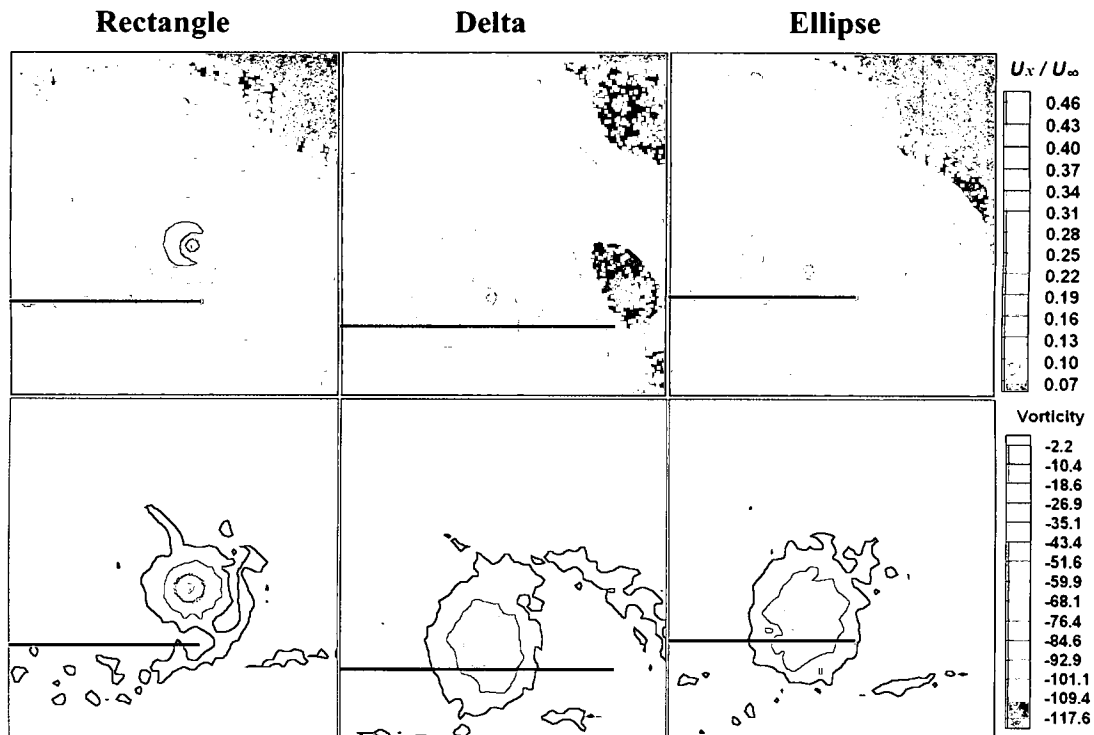


Figure 29: Velocity and Vorticity; 10 deg. AoA; downstream $X/C = 1$; $U_\infty = 27$ cm/s; $Re = 24,083$; DPIV results;

The above results are also similar for all the other angles of attack and are consistent with flow visualization results. The same relationships hold for other angles of attack, such as 15 degrees AoA, as seen in Figure 30, as well as for lower Reynolds numbers as shown in Figure 31, where $U_\infty = 9$ cm/s, translating to $Re \sim 8,000$.

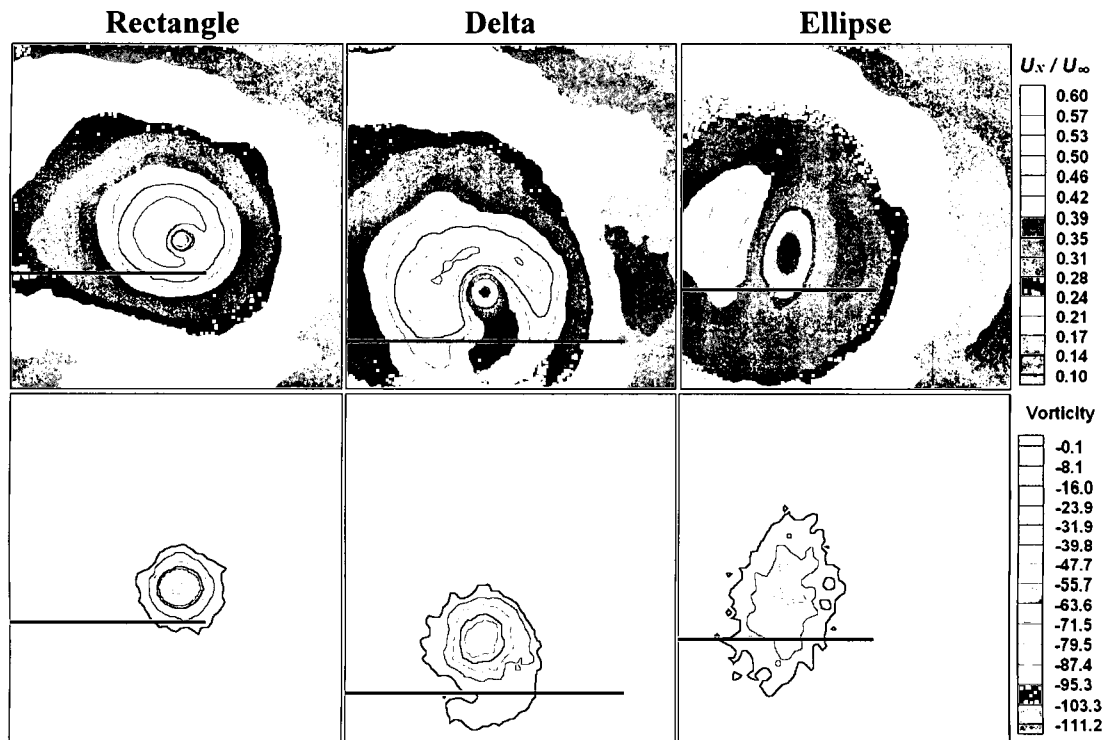


Figure 30: Velocity and Vorticity; 15 deg. AoA; downstream $X/C = 1$; $U_\infty = 27$ cm/s; $Re = 24,083$; DPIV results;

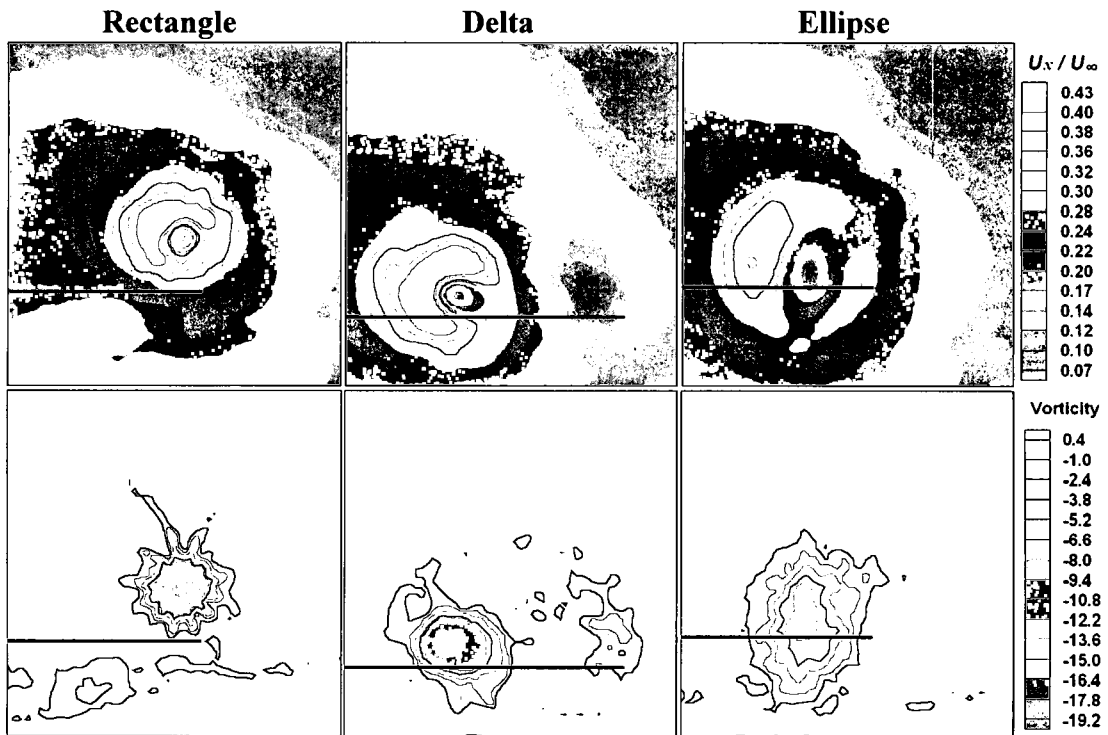


Figure 31: Velocity and Vorticity; 10 deg. AoA; downstream $X/C = 1$; $U_\infty = 9$ cm/s; $Re = 8,028$; DPIV results;

As can be seen from the above images, the vortices are much better structured in the case of the rectangular wing. In fact, in all cases the greatest vorticity is present in the rectangular wing vortex, where the fewest secondary vortices exist. The next largest vorticity is present in delta wing wake, where primary leading edge vortices are dominant. Most likely due to the complex leading edge of the elliptical wing, wing-tip vortices generated by the ellipse are least stable out of all three models. This leads to the smallest averaged tangential velocity values of more than 90 velocity vector fields for each trial. The elliptical wing also produces the most secondary vortices, as can be seen in Figure 32. Thus, the rectangular wing produces the largest tangential velocity, at 15 degrees AoA, on the order of $0.6U_\infty$, compared to delta's $0.5U_\infty$ and ellipse's $0.4U_\infty$ tangential velocities.

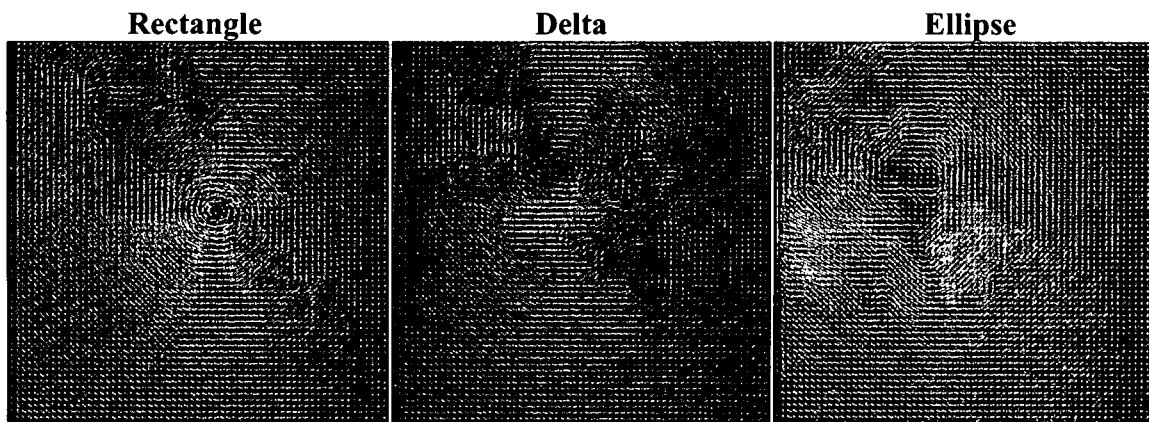


Figure 32: Individual image pairs; 15 deg. AoA; downstream $X/C = 1$; $Re = 24,083$;

Although the fluctuations in the velocity field magnitudes due to these averaging effects are not insignificant, they still have minimal effect on maximum value of circulation, from which coefficients of lift are calculated, as can be seen from Figure 33. Also, there is evidence of wing tip vortices generated by the delta wing, which are seen as vortex “tails” in Figure 30. However, the maximum radius, that was used to obtain maximum circulation values, is large enough to encompass potentially large contribution of the delta wing tip vortex circulation to the overall maximum circulation value.

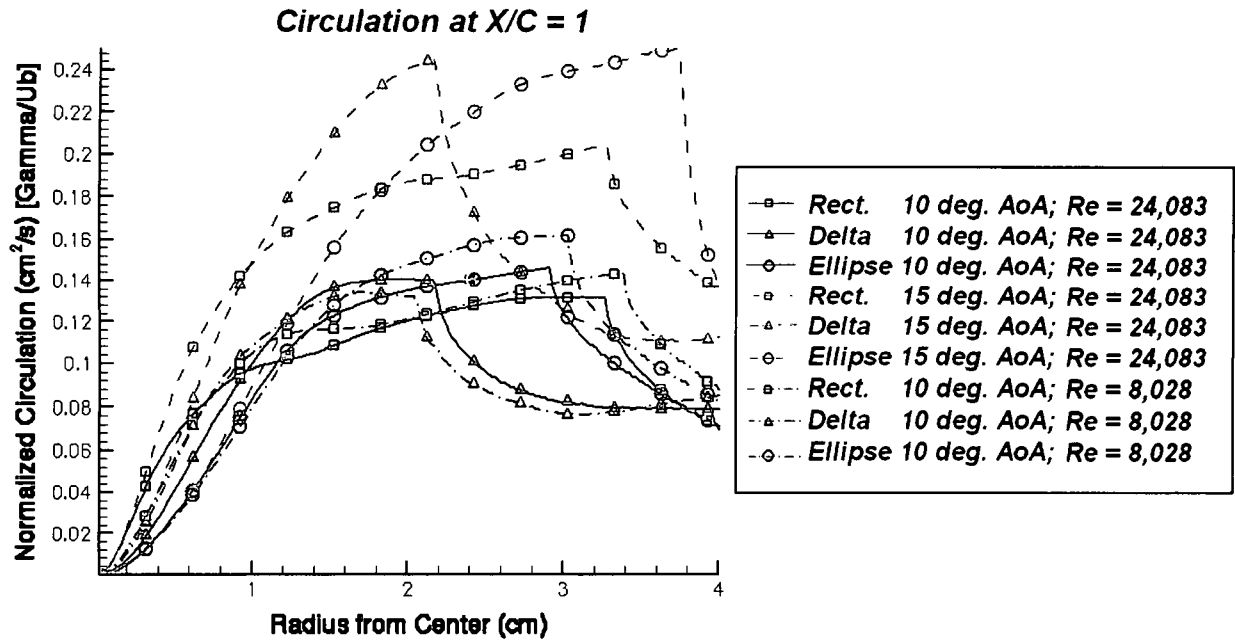


Figure 33: Normalized Circulation at downstream $X/C = 1$;

The decay of the circulation, after the maximum value is obtained at a certain radius from the center of the vortex, is most likely due to the continuation of circulation calculation past the boundary of the image. The change in concavity of the circulation curves, however, is probably due to the potentially significant contribution of the opposite circulation value of secondary vortices.

It is also apparent that although viscosity has a significant effect on the vortex velocity structure downstream of the trailing edge, as can be seen from Figures 34, 35, and 36 below, we can also observe from Figures 37, 38 and 39 that it has virtually no effect on circulation and thus on the coefficient of lift calculations. This fact makes all data, regardless of the distance downstream, relevant for comparison of coefficient of lift and angle of attack relationships even at low Reynolds numbers.

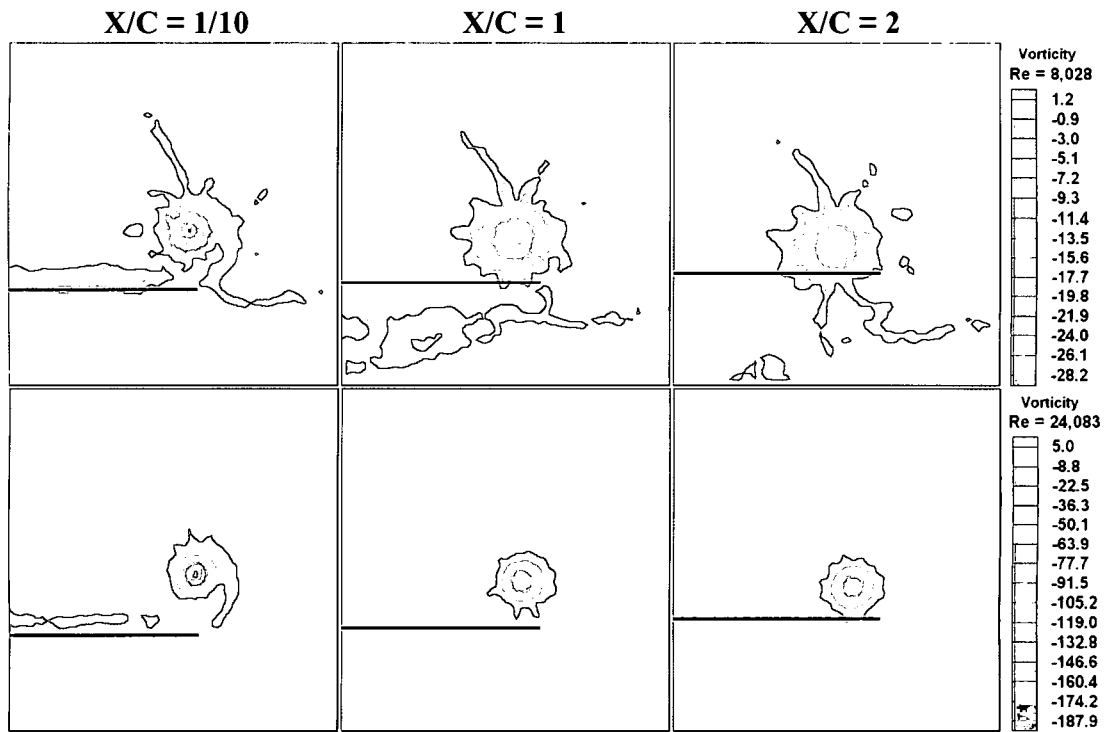


Figure 34: Vortex comparison with distance downstream from trailing edge; Rectangle at 10 deg. AoA;

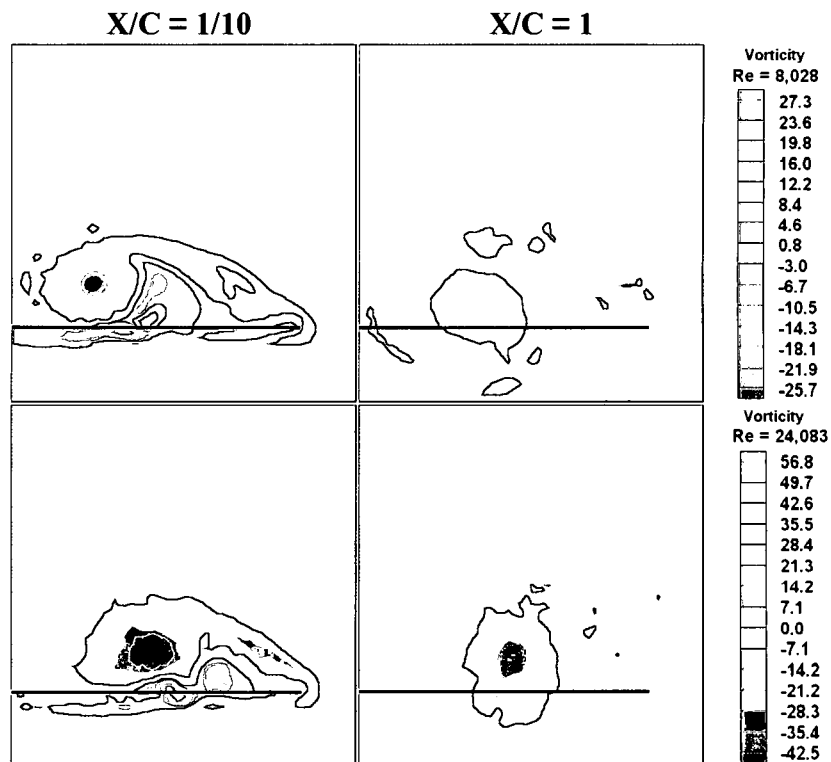


Figure 35: Vortex comparison with distance downstream from trailing edge; Delta at 10 deg. AoA;

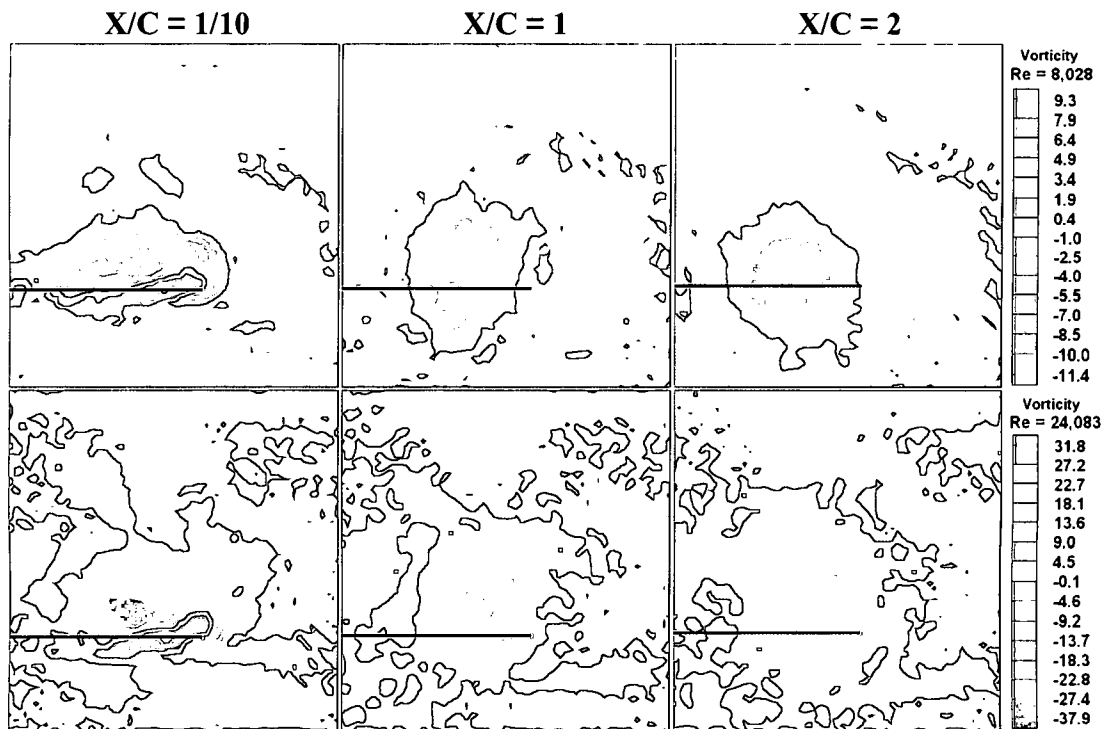


Figure 36: Vortex comparison with distance downstream from trailing edge; Ellipse at 10 deg. AoA;

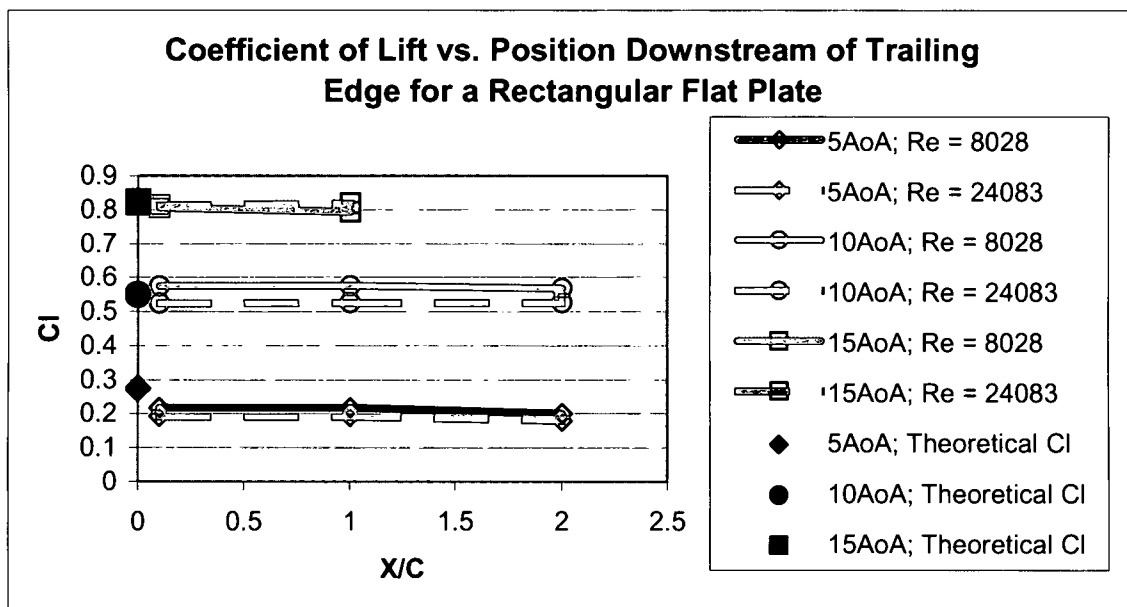


Figure 37: C_l vs. X/C Comparison for Rectangle

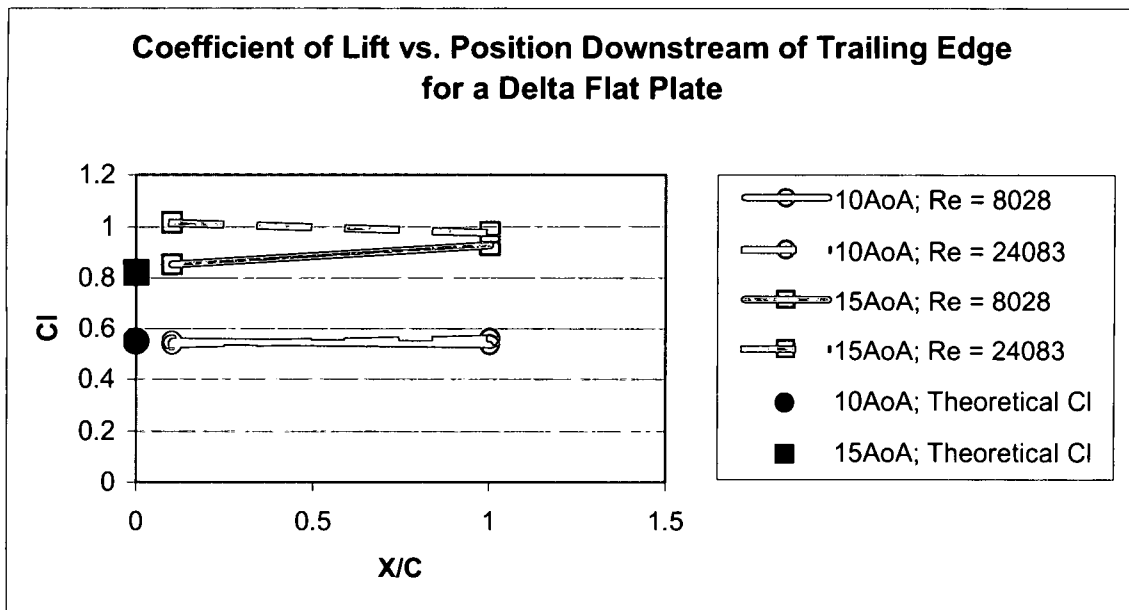


Figure 38: C_l vs. X/C Comparison for Delta

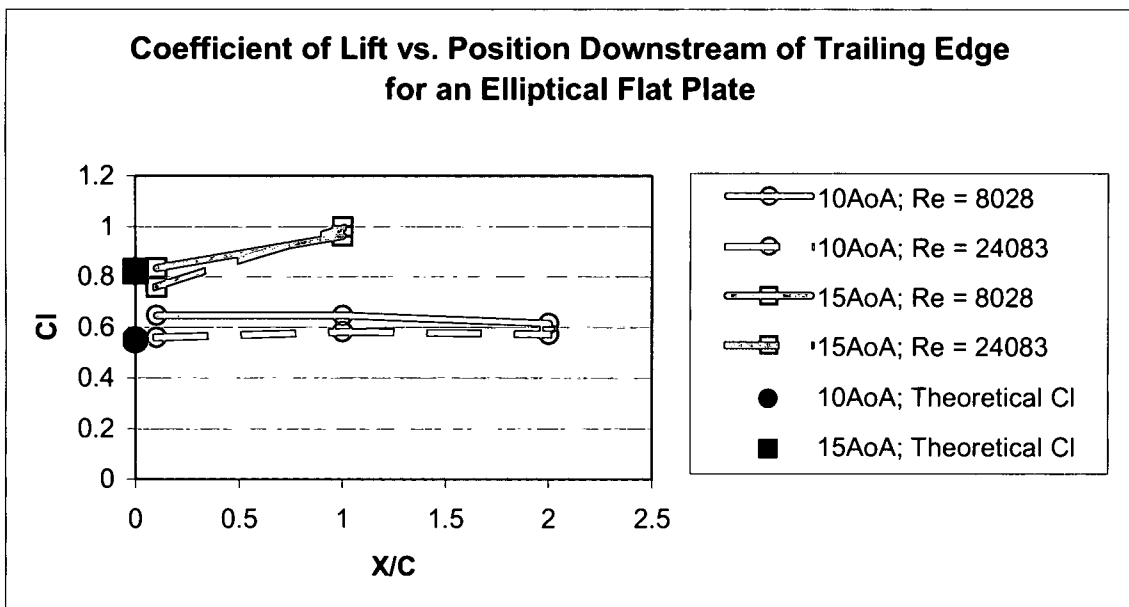


Figure 39: C_l vs. X/C Comparison for Ellipse

The error, where coefficient of lift is actually increased based on the expected decay in circulation with increased distance downstream of the trailing edge, probably comes from averaging all the image pairs for each trial, where once again, the rectangular wing case produces the most stable coefficient of lift. The error for each angle of attack in Figures 37, 38 and 39 is probably also due to the averaging errors of the image pairs,

since there doesn't seem to be any consistency in its behavior based on Reynolds number, or planform geometry. Although the results for the coefficients of lift for the ellipse are less accurate than for the rectangular wing, the error is still acceptable if the results are to be used to make a comparison between the experimentally obtained coefficients of lift and the theoretical predictions. It will also become apparent that the greatest error due to the averaging effects, especially for delta and elliptical planforms, is present at high angles of attack.

An interesting observation can be made regarding the rectangular planform wing tip vortex structure shown in Figures 31 and 34. The vortices produced by the rectangle, at $Re = 8,028$ and in some cases $Re = 24,083$, have 13 spikes, which protrude from the core of the vortex with at least one spike being the largest, and interestingly enough pointed away from the wing tip. This may possibly suggest a very stable vortex structure composed of primary and secondary vortices produced by the rectangular wing. The same phenomenon is visible in the delta wing, which has the second most stable vortices as can be seen in Figure 30. However, in the case of the delta planform, the "tail" that protrudes from the vortex core is most likely a wing tip vortex. This explanation is probably valid since the elliptical wing, with the least stable vortex structure, has the least number of discernable spikes.

The last observation to make before comparing the coefficient of lift and angle of attack relationship is the vortex position relative to the wing tip at different distances downstream from the trailing edge, thus again, inspecting vortex roll-up behavior. After calculating the center of the vortex for each case, vortex position relative to the wing tip is plotted for all three models in Figures 40, 41 and 42.

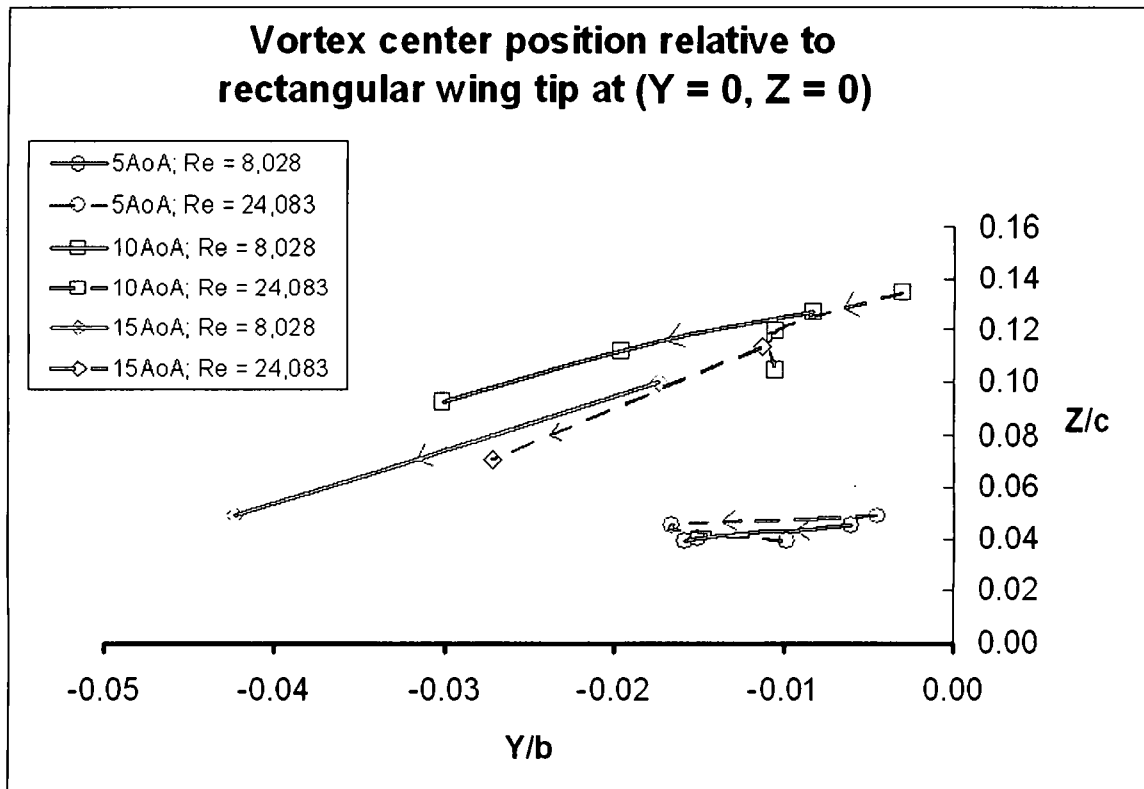


Figure 40: Vortex position downstream of the trailing edge; Rectangle

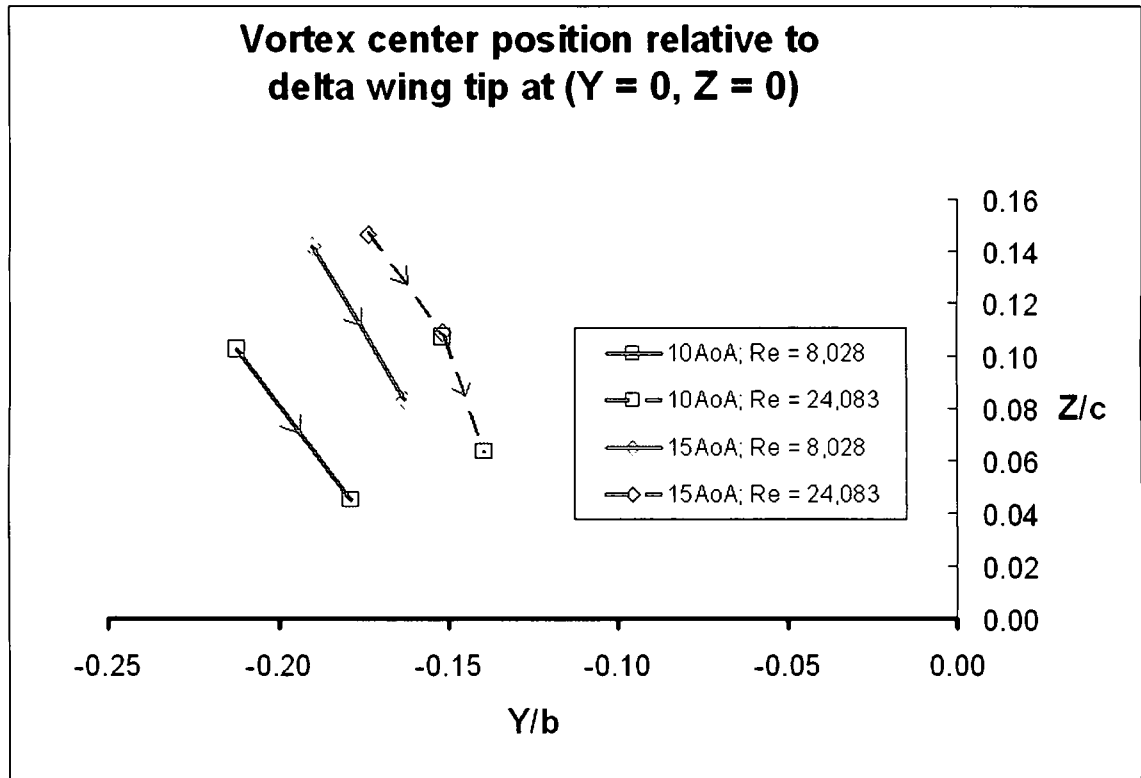


Figure 41: Vortex position downstream of the trailing edge; Delta

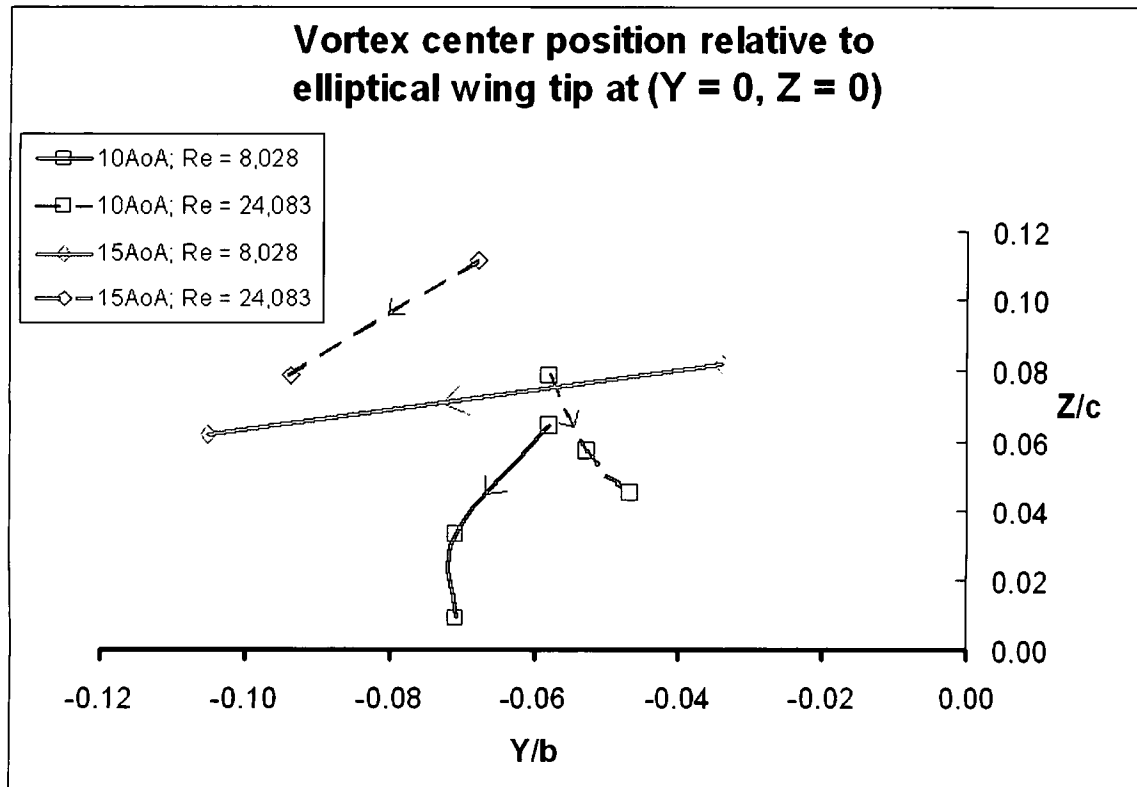


Figure 42: Vortex position downstream of the trailing edge; Ellipse

The direction of the arrows points to the increasing distance downstream from the trailing edge, starting from $X/C = 1/10$. It is apparent that vortex roll-up behavior produced by the rectangular and elliptical flat plates does not mimic high Reynolds number flows. The vortices roll up and towards the root of the wing starting from the wing tip to about a distance of $X/C = 1/10$ downstream from the trailing edge, suggesting a bluff body wake behavior with significantly lower pressure at the top. Due to this low-pressure region on the top of the wing, the vortices initially move upwards. However, from at least $X/C = 1/10$ to $X/C = 2$, vortices slowly move downwards, mimicking high Reynolds number flows. This effect is probably visible due to some residual downwash left over from the wing after the pressure has been equalized between the top and the bottom regions of the wake. However, the rate of change of vortex center location with downstream position is smaller, since both the vertical Z/C and horizontal Y/b position shifts from $X/C = 1/10$ to $X/C = 1$ are smaller than from $X/C = 1$ to $X/C = 2$. Also, for elliptical and rectangular planforms, it is apparent that for the same angle of attack, the low-pressure region on top of the wing is weaker for $U_\infty = 9$ cm/s with $Re = 8,028$, than

for $U_{\infty} = 27$ cm/s, where $Re = 24,083$, resulting in greater vortex displacement from the wing tip in the z -direction, but smaller vortex displacement in the y -direction with an increase in Reynolds number.

$$\text{As } Re \uparrow, \quad Z/c \uparrow, \quad Y/b \downarrow \quad (32)$$

The only exception is for the ellipse at 15 degrees AoA, where the vortex at $Re = 24,083$ is farther from the wing tip in both directions than the vortex generated by the wing at $Re = 8,028$. Thus, the greater the Reynolds number, the greater the roll-up vertical distances, in the z -direction, past the trailing edge. However, at the same Reynolds numbers, the greater the angle of attack, the farther the vortex center position from the wing tip, most likely due to the stronger low-pressure region on the top of the wing at higher angles of attack.

$$\text{As } \alpha \uparrow, \quad Z/c \uparrow, \quad Y/b \uparrow \quad (33)$$

Once again, the exceptions are the ellipse at 15 degrees AoA and rectangle at 15 degrees AoA, where at least the rectangular wing, is possibly past the maximum coefficient of lift angle of attack. It is unknown how the vortices dissipate farther downstream from the trailing edge.

The delta wing, however, produces vortex roll-up behavior similar to the one found at high Reynolds numbers at all positions downstream from the trailing edge, where with an increase in position downstream, the vortices move farther from the root of the wing. This roll-up behavior is most likely due to the fact that the vortices are created at the apex and at the wing tip and are mostly affected by the downwash. Also, since there are fundamental differences in the way deltas produce lift, the low-pressure region on top of the wing is due to the vortex itself over the entire planform. For delta planform, it is evident that with an increase in freestream velocity and thus Reynolds number, the vortex center moves only slightly farther up into the low pressure region, but much closer to the wing tip in the y -direction.

$$\text{As } Re \uparrow, \quad Z/c \uparrow \text{ slightly}, \quad Y/b \downarrow \quad (34)$$

However, with the increase in angle of attack, the vortex center produced by the delta wing moves significantly higher in the z -direction, with virtually no change in position in the horizontal, y -direction.

$$\text{As } \alpha \uparrow, \quad Z/c \uparrow \text{ significantly}, \quad Y/b \uparrow \downarrow \quad (35)$$

All the evidence points to the fact that viscous dissipation of the vortex is not significant and that a comparison can be made between coefficient of lift and angle of attack relationship based on theoretical predictions, with inviscid flow assumptions, and the same relationship based on data obtained from low Reynolds number flows, where viscous forces dominate.

6.c. Coefficient of Lift Comparison

Finally, we compare the actual coefficient of lift and angle of attack relationship in Figures 43, 44 and 45. In all cases, since flat plate wings were used, it is assumed that the coefficient of lift at zero degrees angle of attack is also zero.

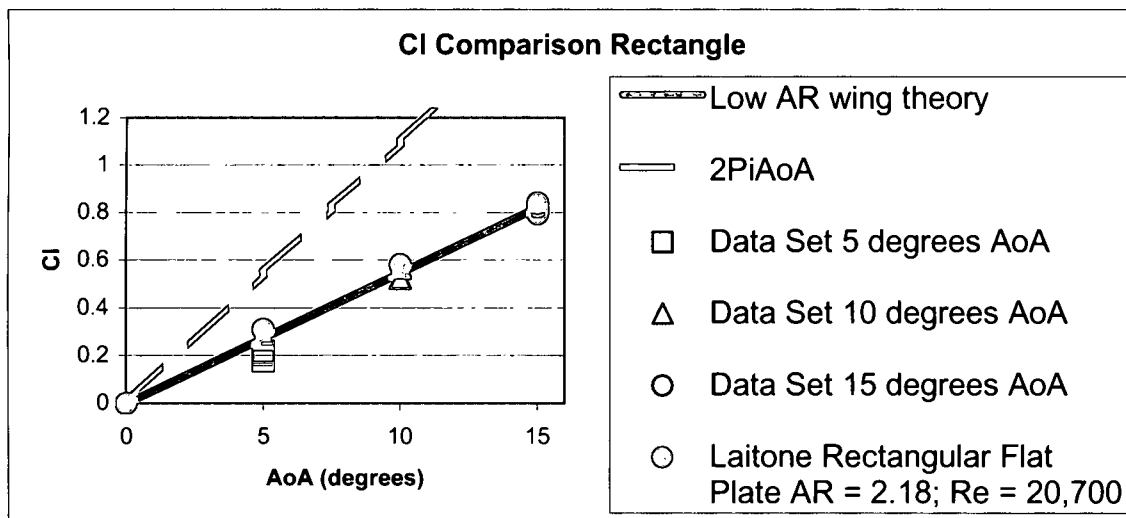


Figure 43: C_l vs. AoA curve; Rectangle

As can be seen in Figure 43, the rectangular wing follows the low aspect ratio theoretical predictions very well, even for the angle of attack of 15 degrees, where at high Reynolds numbers a rectangular flat plate will be very close to stall angle. The only slight disagreement with the theoretical predictions is a relative error on the order of 27% for the rectangular plate at angle of attack of 5 degrees, where the absolute difference in coefficient of lift is ~ 0.074 . Although this error is not due to the averaging effects as discussed earlier, it may be due to the low absolute tangential velocity, from which the vorticity, the circulation and ultimately coefficient of lift are calculated. Finally, as can be seen in Figure 43, the coefficients of lift that were obtained from circulation calculations agree very well with the data gathered with a force balance by Laitone³¹, as

described in Chapter II. In fact, the error between the coefficient of lift based on circulation calculations and the coefficient of lift obtained using a force balance, shown in Table 3, is low enough for flat plate rectangular wings at similar Reynolds numbers and with almost identical aspect ratios, to justify the derivation of the coefficient of lift based on circulation calculated from the trailing edge vortex.

AoA	Cl error					
	5		10		15	
	%	Abs	%	Abs	%	Abs
Rectangle	35.40	-0.110	5.29	-0.031	3.73	-0.031

Table 3: Coefficient of lift error compared to Laitone's force balance measurements

For the delta wing, the results show very good agreement with the swept, low aspect ratio wing theory as discussed in the first Chapter I.

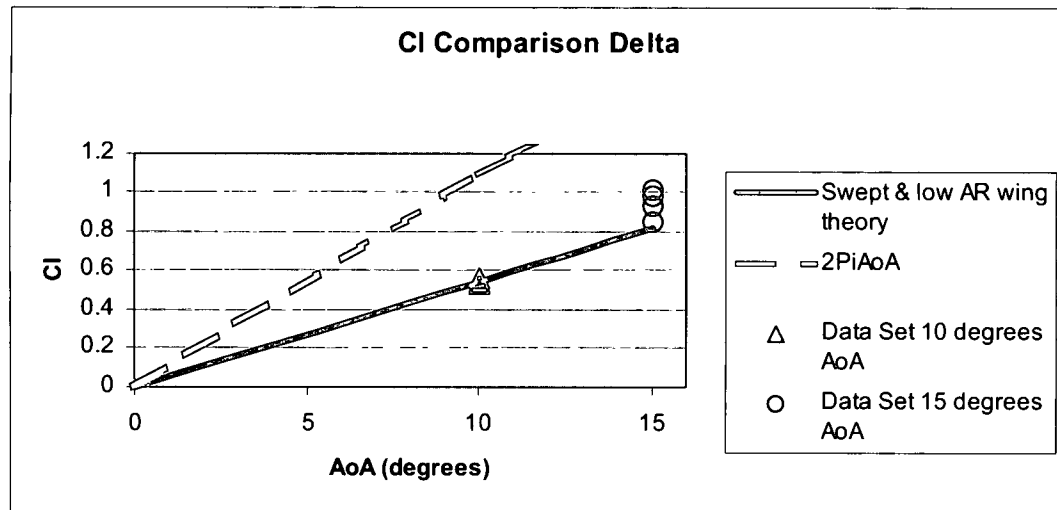


Figure 44: C_l vs. AoA curve; Delta

Here, the greatest error between theoretical approximations and experimentally calculated coefficient of lift is present at 15 degrees angle of attack. The relative error is around 15% and the absolute error in the coefficient of lift is ~ 0.123 . It is very interesting that the error is most pronounced at 15 degrees AoA, since delta wings at high Reynolds numbers stall at higher angles of attack than other planform geometries, such as rectangular or elliptical wings.

Experimentally obtained coefficients of lift for the elliptical planform also agree with the theoretical calculations based on the elliptical lift theory.

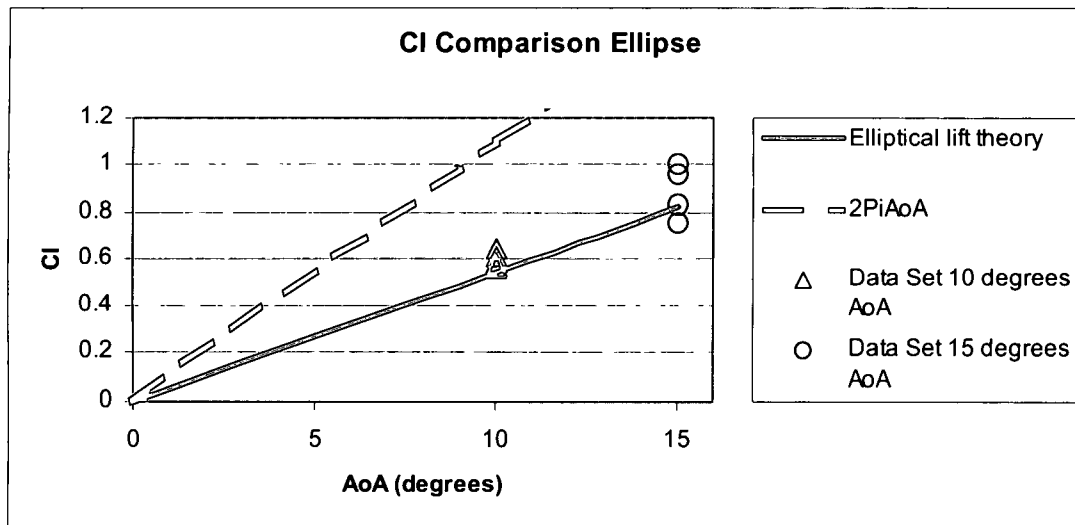


Figure 45: C_l vs. AoA curve; Ellipse

For the ellipse, there is greatest disagreement between elliptical lift theory predictions and experimental data at 15 degrees, similar to the delta wing. At 15 degrees AoA, the absolute error for the coefficient of lift for the ellipse is only ~ 0.067 and the relative error is only 8%, which is actually smaller than the relative error at 10 degrees AoA.

Finally, all the relative and absolute errors between the theoretical and experimentally obtained coefficients of lift are shown in Table 4.

AoA	Cl error					
	5		10		15	
	%	Abs	%	Abs	%	Abs
Rectangle	26.95	-0.074	0.18	0.001	1.67	-0.014
Delta	---	---	0.39	-0.002	15.00	0.123
Ellipse	---	---	10.38	0.057	8.21	0.067

Table 4: Coefficient of lift error compared to theoretical predictions

Since the greatest absolute error is never more than 27% and some differences in coefficient of lift are less than 1%, it is clear that theoretical approximations for each planform that were developed with the inviscid flow assumptions, can also be used to predict lift coefficient in low Reynolds number flows, where once again viscous forces dominate.

The uncertainty in the measurements of the velocity vectors and the calculation of the coefficient of lift is probably within 5%, which results only from averaging more than

90 pairs of individual velocity vectors. The inaccuracy in the calculation of vortex position relative to the wing tip is on the order of 2 pixels, resulting in an uncertainty of ~ 2%. The following chapter discusses the overall observation of vortex behavior and how it relates to the predictions of lift coefficient based on high Reynolds number theories and low Reynolds numbers experimental data.

CHAPTER VII

CONCLUSIONS

As can be seen from the results chapter, the wing that produces the least amount of spanwise flow, which in our case is the rectangular flat plate, produces the most symmetrical and well-defined vortex structure. However, vortex symmetry does not necessarily indicate the largest circulation and therefore lift. Especially, near 10 degrees angle of attack, greatest circulation and therefore coefficients of lift, are produced by the elliptical flat plate, where spanwise flow is maximum, compared to the delta and rectangular planforms. Also as is in the case for high Reynolds number flows, the delta planform seems to produce the largest coefficient of lift at higher angle of attack, such as 15 degrees. At least in this respect, delta flat plate lift generation behavior is similar to the high Reynolds number flows.

It is also very interesting to note that although low Reynolds number flows are in principle dominated by viscous forces and the vortex dissipation should have hampered the selection of distance downstream from the trailing edge in order to get accurate circulation and coefficient of lift representation for each model, in the end as seen from the results chapter, both values did not vary much based on downstream X/C distance. Most of the disagreements in the circulation and coefficient of lift values based on distance downstream of the trailing edge are probably due to the averaging effects of more than 90 velocity fields for each test run and not due to viscous dissipation, at least through $X/C = 2$. This is definitely true for the delta and elliptical wings, where most likely due to the delta's swept leading edge and ellipse's complex leading edge the greatest number of secondary vortices are present as compared to the rectangular wing. However, viscous forces are still strong, regardless of leading edge and planform shape, and have a significant effect on the time and distance required for each vortex to form

into a single symmetrically structured shape. All three models, regardless of freestream velocity or angle of attack produce a fairly symmetrical vortex by $X/C = 2$.

As mentioned before, the stability of vortex center location for all the angles of attack at $Re = 8,000$ and $Re = 24,000$, also seems to be related to the complexity of the leading edge and thus planform. The location of the vortex center is least stable for delta and elliptical wings at low Reynolds numbers, as was observed in each test between more than 90 image pairs. The vortex center seems to fluctuate in the spanwise, y -direction, as well as in the vertical, z -direction to produce dual-core vortices in some cases, which are not present in the individual image pairs, suggesting unstable primary vortex position.

One of the largest disagreements between high and low Reynolds number flows is observed through the location of the vortex relative to the trailing edge and wing tip. Rectangular and elliptical wings at low Reynolds numbers seem to produce vortices that roll up into the low-pressure region, while the delta flat plate produces a vortex that dissipates in a manner similar to the vortices produced by most wings at high Reynolds numbers. The cause of this is unknown. However, it may be due to the fundamental difference of how deltas in general produce lift, and the fact that vortices produced by the delta wing are leading edge vortices created at the apex of the wing, while both the rectangular and elliptical wings produce wing-tip vortices past the trailing edge. This may also help explain the reasons why the predominant vortices produced by the delta wing are located closer to the root of the wing than for rectangular or elliptical planforms. However, the rectangular and elliptical wings even at high Reynolds numbers produce vortices that dissipate downward and away from each other, at least near the ground, which is still the opposite of the case found at low Reynolds numbers.

Despite some of the inaccuracies, that are present due to averaging individual image pairs, as stated earlier, circulation and thus coefficient of lift values are still accurate enough to make comparisons between theoretical predictions of coefficient of lift and angle of attack relationship, based on inviscid flow assumptions, and the same relationship based on experimentally obtained data. The results show that the greatest absolute error between theoretical predictions and experimentally obtained coefficient of lift is 0.123, for a delta at 15 degrees angle of attack, with all the other trials having an error of less than 0.08. This could be due to unpredictability of coefficient of lift near the

stall angle. The largest relative error to the theoretical predictions is 27% for the rectangular planform wing at 5 degrees angle of attack, with the next largest relative error near 15%, present again in delta at 15 degrees. However, taking into account all the other data, the lift curve slope for all three models is very close to π , as predicted in the inviscid flow assumptions. Thus, the same relationships, derived with inviscid flow assumptions and used to predict the coefficient of lift, can be used to at least predict the coefficient of lift for low aspect ratio rectangular, elliptical and delta flat plate planforms in low Reynolds number regimes, between 1,000 and 25,000, where viscous forces dominate.

CHAPTER VIII

RECOMMENDATIONS

This study focused on vortex roll-up behavior, viscous dissipation effects and coefficient of lift production based on planform geometry and angle of attack. The coefficient of lift based on circulation obtained with the help of digital particle image velocimetry was compared to theoretical approximations based on planform geometry and angle of attack with aspect ratio, span, area and mean aerodynamic chord held constant.

The choice of $AR = 2$ resulted in similar predicted lift curve slopes for all three geometries, a rectangle, a delta and an ellipse. Other complex leading edge and planform shapes with the same aspect ratio, span, area and mean aerodynamic chord may be incorporated, to find out if the coefficient of lift and angle of attack relationship at low Reynolds numbers is similar to the one predicted for "inviscid" flows in high Reynolds number regimes. It would be interesting to see if the same relationships would hold for slightly smaller or larger aspect ratios, 1 – 4 as well. Also, the angle of attack of 15 degrees results in the largest error for two out of three models. It would be more appropriate to repeat the study with more refined angle of attack increments near the possible stall angle. For example, a repeat study with angles of attack of 8, 9, ... 14 and 15 degrees would be of interest, especially to identify the stall angle in the same low Reynolds number flow.

Finally, this study is based on an assumption that Kutta-Joukowski theorem extends into low Reynolds number regimes, thus allowing the correlation between the circulation and coefficient of lift. It would be interesting to see if the actual lift force is comparable to the one calculated based on circulation, as is the case for rectangular flat plate from the Laitone study. Force balance measurements for the delta and elliptical wings, would be appropriate to measure the actual lift force produced by the models and see if such correlation still holds.

BIBLIOGRAPHY

-
- ¹ Mueller, Thomas, J., *Fixed and Flapping Wing Aerodynamics for Micro Air Vehicle Applications*, American Institute of Aeronautics and Astronautics, Reston, VA, 2001, p. 5.
 - ² Anderson, Elgin, A., and Todd, A. Lawton: "Correlation Between Vortex Strength and Axial Velocity in a Trailing Vortex," *Journal of Aircraft*, vol. 40, no. 4, July-August 2003, p. 699.
 - ³ Anderson, John D., Jr.: *Fundamentals of Aerodynamics*, 2nd ed., McGraw-Hill Book Company, New York, 1991, p. 126.
 - ⁴ Ibid., p. 129.
 - ⁵ Ibid., p. 136.
 - ⁶ Ibid., p. 137.
 - ⁷ Ibid., p. 216.
 - ⁸ Ibid., p. 262.
 - ⁹ Ibid., p. 264.
 - ¹⁰ Ibid., p. 266.
 - ¹¹ Ibid., p. 272.
 - ¹² Ibid., p. 326.
 - ¹³ Ibid., p. 327.
 - ¹⁴ Ibid., p. 329.
 - ¹⁵ Ibid., p. 343.
 - ¹⁶ Ibid., p. 353.
 - ¹⁷ Ibid., p. 353.
 - ¹⁸ Thwaites, Bryan: *Incompressible Aerodynamics: An Account of the Theory and Observation of the Steady Flow of Incompressible Fluid past Aerofoils, Wings, and Other Bodies*, Dover Publications Inc., New York, 1960, p. 314.
 - ¹⁹ Ibid., p. 316.
 - ²⁰ Ibid., p. 316.
 - ²¹ Federal Aviation Administration: "Aeronautical Information Manual," Aviation Supplies and Academics, Inc., 7005 132nd Place SE, Newcastle WA, 2005, p. 816.
 - ²² Ibid., p. 821.
 - ²³ Anderson and Lawton, p. 702.
 - ²⁴ Lowson, M. V., "Visualization Measurements of Vortex Flows," AIAA paper no. A89-0191, AIAA 27th Aerospace Sciences Meeting, Reno, NV, 1990.
 - ²⁵ Oh, S., and S. Jung: "Experimental Study on the Near Field Structure of Wing-Tip Vortex," AIAA paper no. A00-16635, American Institute of Aeronautics and Astronautics, Reston, VA, 2000.
 - ²⁶ Laitone, E.V., "Wind Tunnel Tests of Wings at Reynolds numbers below 70,000," *Experimental Fluids*, Vol. 23, 1997, pp. 405-409.
 - ²⁷ Zuhail, Lavi, and Morteza, Gharib: "Near Field Dynamics of Wing Tip Vortices," AIAA paper no. A01-31225, American Institute of Aeronautics and Astronautics, Reston, VA, 2001.
 - ²⁸ Jacob, J. D.: "Experimental Investigation of the Trailing Vortex Wake of Rectangular Airfoils," University of California at Berkeley, 1995, p. 175.
 - ²⁹ Ol, M.V.: "The Passage Toward Stall of Non-slender Delta Wings at Low Reynolds Number" California Institute of Technology, 2001.
 - ³⁰ Ol, M.V., Hanff, E.S., McAuliffe, B.R., Scholz, U., and Kaehler, C. "Comparison of Low Reynolds Number Airfoil Laminar Separation Bubble Measurements in Three Facilities". AIAA 2005-5149.
 - ³¹ Mueller, p. 85.

R002592236